3-23-2018

A Comparison of High Frequency Angle of Arrival and Ionosonde Data during a Traveling Ionospheric Disturbance

Kalen L. Knippling

Follow this and additional works at: https://scholar.afit.edu/etd

Part of the Engineering Physics Commons

A COMPARISON OF HIGH FREQUENCY ANGLE OF ARRIVAL AND IONOSONDE DATA DURING A TRAVELING IONOSPHERIC DISTURBANCE

THESIS

Kalen L. Knippling, Captain, USAF

AFIT-ENP-MS-18-M-087

DEPARTMENT OF THE AIR FORCE
AIR UNIVERSITY

AIR FORCE INSTITUTE OF TECHNOLOGY

Wright-Patterson Air Force Base, Ohio

The views expressed in this document are those of the author and do not reflect the official policy or position of the United States Air Force, the United States Department of Defense or the United States Government. This material is declared a work of the U.S. Government and is not subject to copyright protection in the United States.

A COMPARISON OF HIGH FREQUENCY ANGLE OF ARRIVAL AND

IONOSONDE DATA DURING A TRAVELING IONOSPHERIC DISTURBANCE

THESIS

Kalen L. Knippling, B.S., M.A.
Captain, USAF

Committee Membership:

Maj D. J. Emmons, PhD
Chair

Maj O. A. Nava, PhD
Member

Dr. E. V. Dao
Member

Abstract

High Frequency (HF) geolocation techniques are commonly used to track the source of uncooperative HF emitters. A traveling ionospheric disturbance (TID) makes geolocation particularly difficult due to large perturbations in the local ionospheric electron density profile. Angle of Arrival (AoA) and ionosonde virtual height measurements collected at White Sands Missile Range, New Mexico in January 2014, are analyzed during a medium scale traveling ionospheric disturbance. TID characteristics are extracted from the measurements, and a comparison between the data sets is performed to provide a measure of correlation as a function of distance and time between the ionosonde and AoA circuit midpoints. Additionally, ionosonde measurements are used in a simple model to predict AoA elevation angle changes at a downstream HF receiver. The simple model is able to predict changes in AoA elevation angles when the ionosonde North-South tilt is zero; however, as the tilt increases, so too does the error in the simple model.

Acknowledgements

I would like to thank my family and friends for supporting me throughout this project and my career. Additionally, I would like to thank my committee members for your insight, direction, and dedication to my thesis research.

Kalen L. Knippling

Contents

List of Figures

x

xiii

xiv

xv

List of Tables

List of Acronyms

AGW atmospheric gravity wave

AoA Angle of Arrival

DFT discrete Fourier transform

DPS4D Digisonde Portable Sounder 4D

EUV extreme ultraviolet

GIRO Global Ionospheric Radio Observatory

GPS Global Positioning Systems

HF High Frequency

HFGeo HF geolocation

IARPA Intelligence Advanced Research Projects Activity

LSTID large scale traveling ionospheric disturbance

MM mirror model

MSTID medium scale traveling ionospheric disturbance

O-mode ordinary-mode

SSL single station location

TID traveling ionospheric disturbance

UT Universal Time

WSMR White Sands Missile Range

X-mode extraordinary-mode

A COMPARISON OF HIGH FREQUENCY ANGLE OF ARRIVAL AND IONOSONDE DATA DURING A TRAVELING IONOSPHERIC DISTURBANCE

I. Introduction

HF radio communication is an effective and inexpensive means of long-range communication. Because the HF communication path can be predicted if ionospheric conditions are known, U.S. Intelligence Advanced Research Projects Activity (IARPA) and the Department of Defense are interested in being able to determine the exact location of an uncooperative HF transmission using techniques known as geolocation. HF radio waves transmitted via sky wave propagation, reflecting off the ionosphere, extends the the communication distance up to 4000 km [Headrick and Skolnik, 1974]. If the ionosphere were a perfectly smooth, spherically symmetric layer, it would be relatively easy to determine the location of a HF transmitter based on geometry; however, this is unrealistic during a traveling ionospheric disturbance (TID) as oscillations in the ionosphere result in a tilt at the reflection point.

A TID is a form of an atmospheric gravity wave (AGW) that results in a large perturbation in the local ionospheric electron density profile. Because the ionosphere is dynamic, its structure will fluctuate in response to a TID affecting radio wave reflection off the ionosphere and arrival at a HF receiver. Therefore, understanding the real-time effects of TIDs on the ionosphere is vital to geolocation accuracy.

TIDs have been studied since the last half of the 20th century [Hines, 1960, Hunsucker, 1982], and are observed by changes in the ionospheric electron density profile as measured by Global Positioning Systems (GPS), incoherent scatter radars, HF Doppler systems, and ionosondes. From these measurements, TID amplitude, phase,

1

للاستشارات المنارة

www.manaraa.com

and velocity of the wave as a function of the period can be revealed [Ding et al., 2007, Crowley and Rodrigues, 2012, Crowley et al., 2013]. TIDs have periods of 10 minutes to 5 hours, velocities of 50 to $1000\,\mathrm{m\,s^{-1}}$, and wavelengths of 100 to $5000\,\mathrm{km}$ [Crowley et al., 2013]. Measurements from ionosondes also disclose wave variation as a function of height during a TID event [Tedd et al., 1984, Shiokawa et al., 2002].

Measurements from ionosondes, angle of arrival (AoA) a HF signal incident upon a HF receiver, and Doppler frequency shifts have been used to study HF radio communication during a TID. By modeling the ionosphere as a perfectly reflecting surface, AoA and Doppler frequency shift measurements are able to recover TID characteristics [Galushko, 2003, Paznukhov et al., 2012] and extract the direction of propagation [Paznukhov et al., 2012]. Additionally, application of time delay, integrated Doppler shift, and AoA measurements have been incorporated into ionospheric data assimilation algorithm models, such as GPS Ionospheric Inversion model, to successfully model AoA measurements when three known reference points are within $50\,\mathrm{km}$ of a HF transmitter [Nickisch et al., 2016]. AoA elevation angles are dependent on the ionospheric reflection height [McNamara, 1991] and we expect them to be directly correlated.

This research project is focused on the development of a simple model to assist with geolocation techniques. AoA elevation angles and ionosonde virtual height measurements from a 14-day IARPA HF geolocation (HFGeo) field campaign at White Sands Missile Range (WSMR), in January 2014, are analyzed to extract TID characteristics. A comparison between the two data sets is performed to reveal the correlation as a function of distance and time between the ionosonde and AoA circuit midpoint. Finally, a simple model is developed that applies ionosonde virtual height measurements to predict AoA elevation angle changes at a downstream HF receiver.

This document is outlined as follows: Chapter II provides background information

on the ionosphere, ionosonde, TIDs, and HF geolocation. Chapter III discusses the methodology and results of this research. The correlation between AoA elevation angle and ionosonde virtual height measurements is performed. A spectral analysis is used to reveal TID wave characteristics. TID velocity is computed from ionogram and spectral analysis phase differences between ionosondes. A temporal cross-correlation estimates the time a TID impacts an AoA circuit midpoint and how the wave structure changes over distance. Finally, a simple model is used to predict changes in AoA elevation angles. Lastly, Chapter IV provides the findings and recommendations for future research with this data set.

II. Background

2.1. Ionosphere

To gain an understanding of TIDs and the impact they pose to geolocation, we must understand the ionospheric layer in which TIDs propagate. The ionosphere is the iononized layer of Earth's upper atmosphere that extends from 50 to 1000 km [Pisacane, 2008], and is responsible for the refraction of HF radio waves. Plasma in this region forms primarily by the photoionization of the neutral constituents by extreme ultraviolet (EUV) and x-ray radiation in low and mid-latitudes [Schunk and Nagy, 2009]. The ionosphere is subdivided into regions based on local peaks in electron density distributions. The maximum electron density occurs at the F2 peak located at approximately 300 km; however, the electron density profile changes with diurnal, seasonal, latitudinal and solar cycle variations, as depicted in Figure 1 [Schunk and Nagy, 2009].
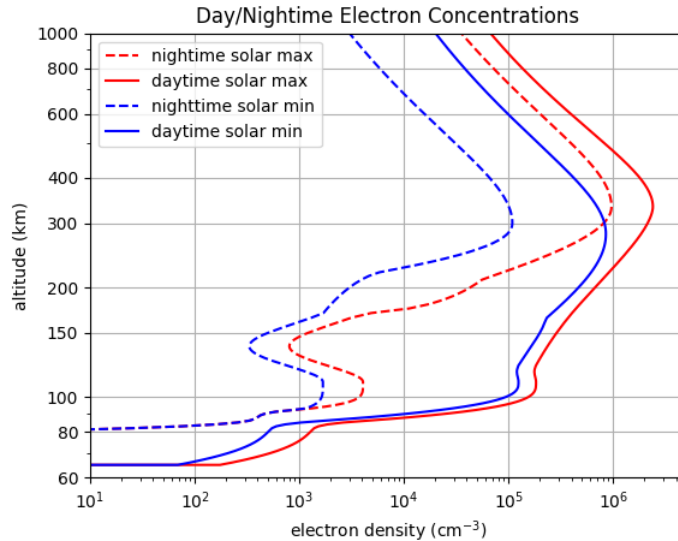
Figure 1. Ionospheric electron density profile as a function of altitude [Dao, 2018]. This reveals the diurnal and solar cycle variations in the electron density profile.

The lowest subregion, the D region, extends from 50 to 90 km above Earth's surface, and is formed by photoionization from solar Lyman alpha and hard x-rays [Pisacane, 2008]. The D region is comprised of molecular ions, positive and negative ions, and water cluster ions, with NO^+ and O_2^+ as the major constituents [Schunk and Nagy, 2009]. The maximum electron density, $10^9\,m^{-3}$, is reached shortly after sunrise and reduces significantly after sunset, $10^2\,m^{-3}$, when the primary ionization source, the sun, is lost [Pisacane, 2008].

The E region spans from 90 to 150 km and is primarily formed by photoionization from x-ray and ultraviolet radiation, and the dominant ions are NO^+, O^+, O_2^+, and N_2^+ [Pisacane, 2008]. During the day, the electron density peaks at $10^{11}\,m^{-3}$, near 120 km [Pisacane, 2008]. Similar to the D region, after sunset when the primary source of ionization is lost, the electron density decreases to $2 \times 10^9\,m^{-3}$ [Pisacane, 2008].

The F region stretches from 120 to 1000 km, and is formed by photoionization from EUV radiation with O in the lower levels and H in the upper levels [Pisacane, 2008]. During the day the F region forms two distinct layers, F1 and F2. The F1 layer extends from 120 to 200 km, with a peak electron density of $2 - 5 \times 10^{11}\,m^{-3}$ near 180 km [Pisacane, 2008]. The F2 layer spans from 200 to 1000 km and has a peak electron density of $1 - 2 \times 10^{12}\,m^{-3}$ at approximately 300 km [Pisacane, 2008]. At night when the ionization source is lost, the two layers merge into one, and the peak electron density decreases to $2 - 5 \times 10^{11}\,m^{-3}$ near 300 km [Pisacane, 2008].

The ionosphere electron densities are important to HF radio communication because the plasma refracts and reflects radio waves. For reflection to occur, the frequency of the radio wave must not exceed the plasma (critical) frequency,

$$f_p = 8.979\sqrt{n_e} \qquad (1)$$

where f_p is plasma frequency (Hz) and n_e is number density of electrons (m^{-3})

[Pisacane, 2008]. When radio transmissions occur at frequencies much less than the vertical incidence F2 plasma frequency, the wave will reflect off the ionosphere at lower altitudes, reducing the distance the wave travels [Pisacane, 2008]. However, transmissions at vertical incidence frequencies greater than the F2 plasma frequency, will penetrate the ionosphere and the wave will not return back to Earth [Pisacane, 2008]. Table 1 outlines the plasma frequency for each region of the ionosphere, as calculated from Equation 1, given the peak electron density for the respective region [Pisacane, 2008].

Table 1. A list of plasma frequencies for ionospheric regions.

Region	Altitude (km)	Electron Density (m^{-3})	Plasma Frequency (MHz)
D	50 - 90	10^2 (night) 10^9 (day)	9×10^{-5} 0.3
E	90 - 150	2×10^9 (night) 10^{11} (day)	0.4 3
F1	120 - 200	2×10^{11}	4
F2	200 - 1000	2.5×10^{11} (night) 1.5×10^{12} (day)	4.5 11

2.2. Ionosondes and Angle of Arrival Measurements

An ionosonde is a ground-based HF radar system that measures the ionosphere. The ionosonde transmits a radio pulse vertically across a range of frequencies and measures the time delay of the return signal in order to calculate the electron density as a function of altitude [LDI, 2009]. Radio waves travel at a group velocity proportional to the index of refraction and reflect off the ionosphere when the group velocity is equal to zero; thus, the frequency of the transmitted radio wave must equal the

6

plasma frequency [LDI, 2009, Pisacane, 2008],

$$v_g = c\sqrt{1 - \frac{f_p^2}{f^2}} \tag{2}$$

where v_g is group velocity $(\mathrm{m\,s^{-1}})$, c is vacuum speed of light $(\mathrm{m\,s^{-1}})$, and f is the radio frequency (Hz). Given this, the electron density at the reflection altitude is derived for each frequency by

$$\begin{aligned} n_e &= \left(\frac{4\pi^2 \epsilon_0 m_e}{e^2}\right) f_p^2 \\ &= \frac{f_p^2}{80.62} \end{aligned} \tag{3}$$

where n_e is electron density $(\mathrm{m^{-3}})$, ϵ_0 is permeability of free space $(\mathrm{C^2\,s^4\,m^{-4}\,kg^{-2}})$, m_e is mass of an electron (kg), and e^2 is charge of an electron (C) [Pisacane, 2008].

The above description for which the group velocity is proportional to the index of refraction, excludes the complicating factor of the Earth's magnetic field. The application of Earth's magnetic field through the Appleton-Hartree Equation, reveals the ionosphere contains two indices of refraction, n,

$$n^2 = 1 - \frac{X}{1 - \frac{(Y\sin\Psi)^2}{2(1-X)} \pm \sqrt{\frac{(Y\sin\Psi)^4}{4(1-X)^2} + (Y\cos\Psi)^2}} \tag{4}$$

where $X = f_p^2/f^2$, $Y = f_g/f$, Ψ is the angle between the wave's k vector and the background magnetic field, f_p is the plasma frequency, f is the frequency of the wave, and f_g is the electron gyrofrequency [Davies, 1990]. Therefore, a transmitted wave contains two polarized components, an ordinary-mode (O-mode) and extraordinary-mode (X-mode) wave. The index of refraction for the O-mode occurs when the $\pm$ in Equation 4 is positive, and the X-mode when the $\pm$ is negative. Since the index of refraction is related to the group velocity, the O-mode and X-mode waves propagate

المنارة للاستشارات

www.manaraa.com

at different speeds and return separate signals to the ionosonde receiver [LDI, 2009], as shown on the ionogram in Figure 2.

One of the products the ionosonde produces is the ionogram. The ionogram is a six-dimensional measurement of signal amplitude versus frequency, and signal amplitude versus altitude [LDI, 2009]. The six-dimensional measurements comprise the frequency, virtual reflection height, signal amplitude, polarization, Doppler shift, and AoA [LDI, 2009]. Figure 2 shows an ionogram from the Cherry ionosonde on 26 January 2014 at 1934 Universal Time (UT). The product contains a wealth of information from computer scaled ionospheric parameters to the distance a wave will travel if transmitted at the maximum usable frequency [LDI, 2009]. The center graph depicts the virtual reflection height of a transmitted frequency for both the O-mode wave in red, and the X-mode wave in green [LDI, 2009]. The virtual reflection height is greater than the actual reflection height because the virtual height does not account for the refraction of the wave as the electron density increases, but instead is determined by the group velocity (Equation 2) traveling slower than the speed of light, and approaches zero near where the plasma frequency is equal to the transmission frequency. From the ionogram, the electron density as a function of altitude can be found by Equation 3. In Figure 2, the weaker signatures at higher altitudes above a very predominate layer, represent a second return echo from the initial radio transmission [LDI, 2009]. Additionally, the ionogram reveals perturbations in the electron density profile which indicate the onset of a TID, as shown by the circled cusp, or hook in the O-mode profile in Figure 2. Finally, a color scale provides details on the AoA where cold shades indicate a return signal from the North to East and warm shades from the South to West.

AoA measurements from the WSMR field campaign relied on an HF receive array tuned to receive 10 HF transmitters fielded for the geolocation experiment. The

8

Auto-scaled parameters

foF2	8.225
foF1	4.61
foFlp	3.99
foE	3.16
foEp	2.96
fxI	8.80
foEs	3.15
fmin	2.25
MUF(D)	25.42
M(D)	3.10
D	3000.0
h'F	216.0
h'F2	228.0
h'E	100.0
h'Es	100.0
hmF2	277.1
hmF1	180.4
hmE	99.2
yF2	116.7
yF1	8.0
yE	8.9
B0	104.1
B1	4.04
C-level	11

Auto:
Artist4.5
200311

Statio YYYY DAY   DDD HHMM P1 FFS S AXN PPS IGA PS
Cherry 2014 Jan26 026 1934 RSF 050 4 713 200 01+ A1

Hook

2nd Hop

O-mode   X-mode

E Layer

AoA information gained through beamforming

NNE
E
W
Vo-
Vo+
SSW
X-
X+
SSE
NNW

Auto-scaled profile (topside is a guess)

Frequency (MHz)

D   100 200 400 600 800 1000 1500 3000 [km]
MUF 8.8 8.9 9.3 9.9 10.8 12.1 15.9 25.4 [MHz]
CH833 2014026193400.RSF / 176fx128h 50 kHz 5.0 km / DPS-4 CH833 993 / 32.9 N 253.6 E   Ion2Png v. 1.1.03

Figure 2. Example of an ionogram. Ionogram from Cherry ionosonde measurements on 26 January 2014 at 1934 UT. Notice the hook in the O-mode profile, between 8-9 MHz at 600-640 km; this indicates the onset of a TID.

transmit antennas were primarily single inverted-V dipole with one transmitter as a two antenna inverted-V dipole [Munton et al., 2016]. These transmitters disseminate signals in linear frequency chirp and swept sounder mode emitting signals at 3 to 12 MHz [Munton et al., 2016]. The receive array consists of one radio per dipole with three channels per radio set-up across the 19 inverted-V cross dipole antennas to make up an array with an aperture of about $200\,\mathrm{m}^2$ [Dao, 2018]. As a HF radio wave is emitted, the wave incident upon the antenna array arrives at an angle, with each individual antenna in the array receiving the signal at a different time as a function of the AoA. Based on the direction the radio wave propagates from, the individual antenna within the receive array that is closest to the source will receive the signal prior to the other antennas within the array [Dao, 2018]. Given the direction by which the radio wave arrives at each individual antenna and a known wavelength, the AoA is inferred by how out of phase the radio wave is at each antenna relative to

9

the other antennas within the receive array [Dao, 2018, Munton et al., 2016]. AoA measurements provide the azimuth and elevation angle of a radio wave reflected off the ionosphere and incident upon the receiver. AoA measurements from two WSMR sites are displayed in Figure 3 to illustrate how the azimuth and elevation angles vary over time. The AoA elevation angle at G10-RDS1 is approximately 5° greater than G10-N1, which indicates that the ionospheric reflection point is higher at the G10-RDS1 circuit midpoint.

The specific ionosondes in use during the WSMR field campaign were the Digisonde Portable Sounder 4D (DPS4D) at Kirtland, Munyo, and Squirt, and an older model, DPS4, at Cherry; both produced by Lowell Digisonde International. The DPS4D utilizes a Turnstile delta transmitter antenna to scan frequencies from 0.5 to 30 MHz, in increments of 1 kHz and four active crossed loop Turnstile antennas as receivers [LDI, 2009]. The signal processor requires two embedded Intel Core 2 Duo Dual Core processors, which include seven operating modes that allow for alternating transmissions of ordinary and extraordinary wave polarizations [LDI, 2009]. The DPS4D enables ionospheric measurements from 0 to 1200 km with a height resolution of 5 km [Dao, 2018, LDI, 2009]. For a comprehensive list of the DPS4D specifications, reference the technical manual published by Lowell Digisonde International.
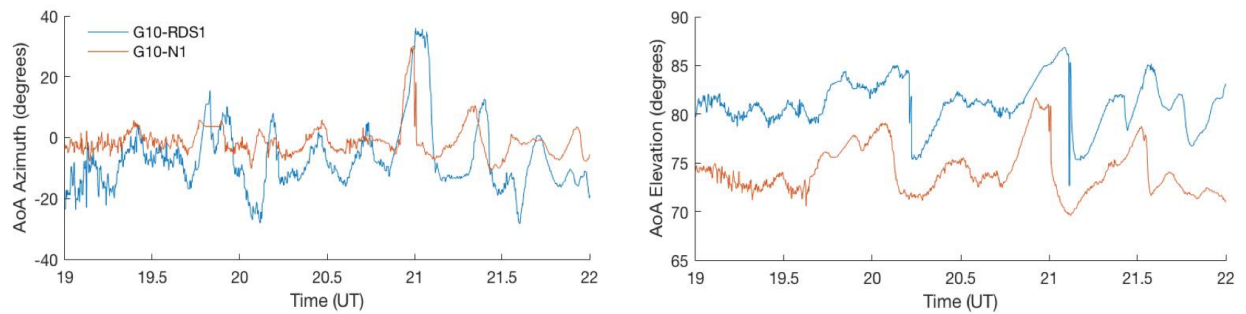
Figure 3. Example plot of AoA measurements for G10-RDS1 and G10-N1. Left: AoA azimuth angle versus time. Right: AoA elevation angle versus time.

10

The January 2014 WSMR field campaign had four ionosondes within a 300 km range that measured the ionosphere every 2 to 6 minutes. This proximity and sampling cadence is not normally available around the world. As of 2011, there were 64 ionosonde locations worldwide collecting ionospheric measurements in 33 countries [Galkin and Reinisch, 2011]. Figure 4 shows the global ionosonde coverage as of May 2017 [Reinisch, 2017]. Typical ionospheric measurements from these locations take place every 15 minutes, with measurements stored on the Global Ionospheric Radio Observatory (GIRO) portal. This information is used by operators and ingested into ionospheric and space weather forecast models [Galkin and Reinisch, 2011] to enhance geolocation accuracy.
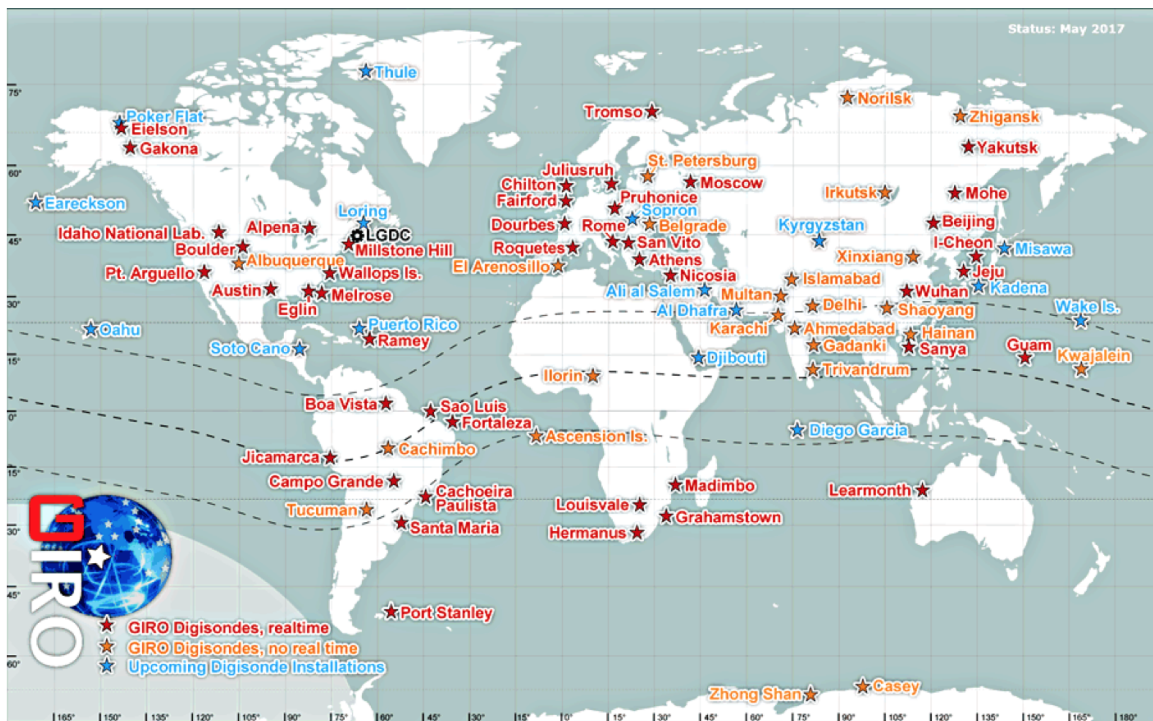
Figure 4. Global Map of GIRO Digisondes as of May 2017 [Reinisch, 2017]

2.3. Traveling Ionospheric Disturbances

Ionosondes and other ionospheric measuring instruments can be used to study TIDs. TIDs are typically observed in the F region and result from perturbations in the electron density profile as a result of an atmospheric gravity wave (AGW). AGWs are oscillations of the neutral atmosphere that transfer energy and momentum from low to high altitudes, or high to low ionospheric latitudes [Crowley et al., 2013]. AGWs occur when dense air is perturbed and rises above less dense air, causing an unstable layer which gravity attempts to restore [Hocking, 2001]. This interaction initiates an oscillation in the wave, and the wave amplitude increases with vertical propagation due to the conservation of energy per unit volume [Hocking, 2001]. In other words, as the wave propagates higher in altitude where the density is less, the velocity of the oscillation must increase to conserve energy; thus, the amplitude of the wave increases with altitude as depicted in Figure 5 [Hines, 1960, Hocking, 2001].

AGWs generated from low to high altitudes, stem from tropospheric events such as thunderstorms, airflow over mountains, and volcanoes [Schunk and Nagy, 2009]. Additionally, studies on tropical storm systems have found these large convective storms release enormous amounts of energy which generate horizontally propagating AGWs [Walterscheid et al., 2003]. AGWs generated from auroral processes, which transfer energy and momentum from high to low ionospheric latitudes, include Joule heating, Lorentz forces, and intense particle precipitation events [Hunsucker, 1982].

TIDs are classified as medium scale traveling ionospheric disturbance (MSTID) or large scale traveling ionospheric disturbance (LSTID) based on size, period, and velocity of the wave. MSTIDs are characterized to have: wavelengths of several hundred kilometers, periods of tens of minutes to an hour, and phase velocities of 50 to $300\,\mathrm{m\,s^{-1}}$[Crowley et al., 2013]. The behavior of MSTIDs also vary based on time of day, requiring a daytime or nighttime designation [Otsuka et al., 2013]. Daytime

12
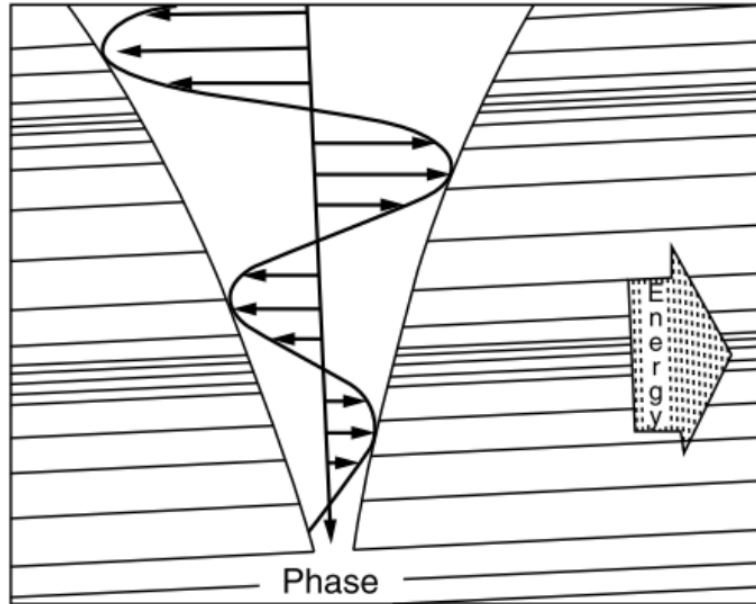
Figure 5. Representation of an AGW. Arrows represent the neutral velocity variation with altitude while density variations are depicted by parallel lines lying in surfaces of constant phase. The AGW phase progression is downward, energy propagation to the right, and gravity is directed vertically downward. [Hines, 1960] [©] **2008 Canadian Science Publishing or its licensor. Reproduced with permission.**

MSTIDs typically occur during the winter months and travel equatorward, suggesting the source is the oscillation of neutral gases produced by AGWs [Otsuka et al., 2013]. This occurs when neutral gases collide with ions in the F region that force plasma to move along Earth's magnetic field lines, because the collision frequency is less than the gyrofrequency [Otsuka et al., 2013]. As the neutral winds change direction with altitude due to the oscillatory nature of the wave, plasma either converges or diverges along the magnetic field lines [Kelley, 2009]. As plasma converges along the field line, the plasma density increases, and as the plasma diverges along the magnetic field line, the plasma density decreases [Kelley, 2009].

Nighttime MSTIDs vary based on season and latitude, with the direction of propagation to the southwest with large variations in the total electron content [Otsuka et al., 2013, Crowley et al., 2013]. Given the southwestward propagation is not consistent with typical AGWs, researchers suggest that electrodynamic forces

13

such as the polarization electric field may play a role in the generation of nighttime MSTIDs [Otsuka et al., 2013].

Characteristics of LSTIDs include: wavelengths of several hundred to 5000 km, periods of 1 to 5 hours, and a phase velocity of 300 to 1000 m s^{-1} [Crowley et al., 2013]. These waves typically propagate from polar to equatorial regions, suggesting that auroral heating may play a role in the generation of LSTIDs [Crowley et al., 2013]. In a study of LSTIDs during geomagnetic storms on 29-30 October 2003, researchers investigated three LSTIDs that passed over the United States [Ding et al., 2007]. The storms traveled southwestward approximately 2000 km in 1 to 2 hours, with the source of the first two LSTIDs believed to be the auroral westward electroject, while the source of the third LSTID remains unknown [Ding et al., 2007].

2.4. High Frequency Geolocation

HF geolocation is the ability to use AoA measurements to track the source of an uncooperative HF transmitter in which the searching agency does not have control over the device [McNamara, 1991]. Geolocation plays an important role in law enforcement, military, and intelligence operations, when the only information available to operators are the AoA measurements collected at the receiver.

Sky wave radio propagation occurs when a HF transmitter emits a radio wave through the atmosphere and the wave refracts off the ionosphere to return to Earth, where the signal arrives at the receiver as Figure 6 shows. The wave incident upon the receiver contains AoA measurements that allow researchers to select a method to estimate the coordinates of the transmitter. The method chosen depends on the approximate range between the transmitter and receiver circuit; long range circuits (greater than 800 km) rely on ray re-tracing programs which employ ionosphere models, medium range circuits (400 to 800 km) use the single station location (SSL)

14
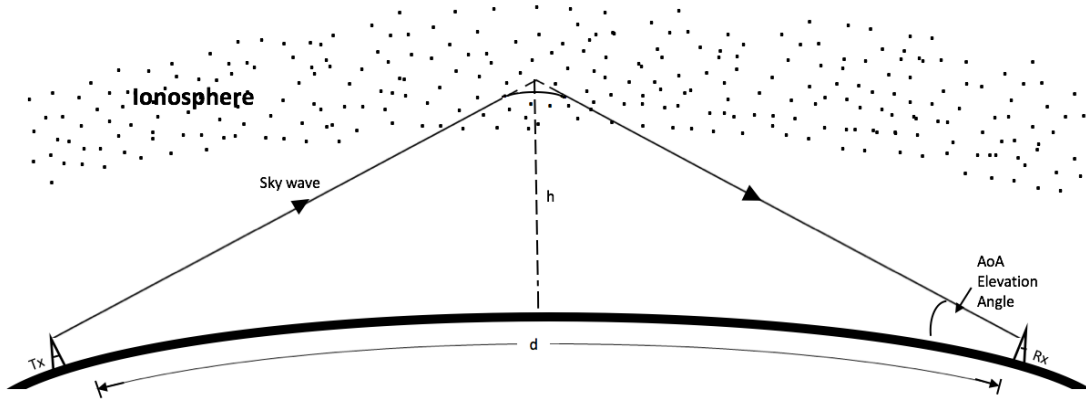
Figure 6. Illustration of sky wave radio propagation between transmitter (Tx) and receiver (Rx), as rendered from McNamara [1991].

method, and short range circuits (less than 400 km) apply the SSL method with a tilted reflection point [McNamara, 1991]. For the purposes of this research, the SSL method is selected.

The SSL method treats the ionosphere as a perfectly smooth surface, much like a horizontal mirror at the reflection point; hence, it may also be referred to as the mirror model (MM) method. The SSL method relies on the secant law, Breit and Tuve's theorem, and Martyn's equivalent path theorem [McNamara, 1991]. This method assumes a transmitted radio wave forms an isosceles triangle between the transmitter, ionospheric reflection point, and receiver as illustrated in Figure 7. Therefore, if the elevation angle, ϵ, of the wave incident upon the receiver, and the height, h, at the ionospheric reflection point for the equivalent vertical frequency from a nearby ionogram are known, the distance between transmitter and receiver, d, is

$$d = \frac{2h}{\tan(\epsilon)} \tag{5}$$

[McNamara, 1991]. Variations of Equation 5 are used in this research project when the MM method is referenced; however, it should be noted that this equation does

15
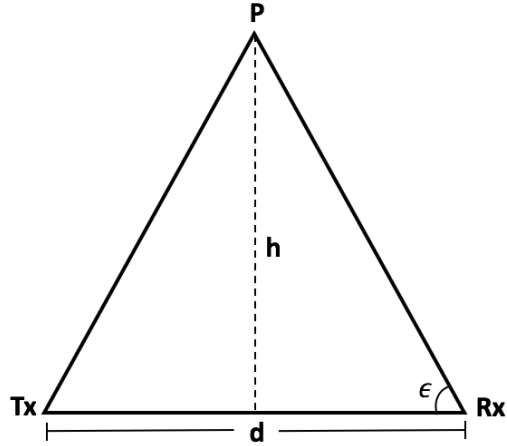
Figure 7. Geometry of the SSL method as rendered from McNamara [1991]. The SSL method treats the ionosphere as a horizontal mirror, which perfectly reflects a sky wave radio signal at the ionospheric reflection point, P, between the transmitter, Tx, and receiver, Rx, separated by distance, d, where h is the height at the reflection point from a nearby ionogram and ϵ is the elevation angle of the wave incident upon the receiver.

not account for the curvature of the Earth or tilts in the ionosphere. For more details on curved Earth calculations, reference McNamara [1991].

The strength of the SSL method resides in the ability to provide quick distance estimates. Because the reflection height is provided via a nearby ionogram, the calculation does not require ray re-tracing or ionospheric model computations [McNamara, 1991]. Despite the speed, the SSL method is not without fault. As noted above, the SSL method does not account for the curvature of the Earth. Additionally, if the AoA elevation angle is less than $50°$, the reliability of the ionogram to estimate the reflection height is no longer reliable [McNamara, 1991]. Finally, the SSL method ignores Earth's magnetic field, which is not realistic [McNamara, 1991].

The SSL method ignores Earth's magnetic field by setting Y, in Equation 4, equal to zero [Dao et al., 2016]. While this makes the calculation easy, it is not practical as Earth's magnetic field is present, as indicated by the O-mode and X-mode trace

16

lines on the ionogram as displayed in Figure 2 [McNamara, 1991]. Neglecting Earth's magnetic field results in geolocation errors of 0 to 35 km in the O-mode, and 0 to 50 km in the X-mode, over ground ranges of 20 to 1000 km [Dao et al., 2016].

When the SSL method is used for short range circuits (less than 400 km), the reflection point is no longer assumed to be a horizontal reflecting surface, but now incorporates a tilt angle [McNamara, 1991]. The tilt at the reflection point is caused by a horizontal gradient in the electron density, which creates a significant error in the calculated distance between transmitter and receiver when using MM without tilts [McNamara, 1991]. The relative error due to a tilted ionosphere is

$$\frac{\Delta d}{d} = \frac{-1.75\Theta}{\sin(\epsilon)\cos(\epsilon)} \tag{6}$$

where Δd is the error in distance d, d is the distance between transmitter and receiver, Θ is the tilt angle (deg) in the direction of propagation, and ϵ is the elevation angle at the receiver [McNamara, 1991]. McNamara [1991] found when the elevation angle was 85°, the relative error was 20% per degree of tilt; however, when the elevation angle lowered to 70°, the error dropped to 5% per degree of tilt, highlighting the importance of the ionospheric tilt angle in short range circuits.

17

III. Methodology and Results

3.1. IARPA HFGeo Field Campaign

In January 2014, a 14 day field campaign took place at WSMR to collect measurements of the ionosphere. By understanding the structure of the ionosphere, particularly in response to a TID, geolocation techniques can be improved. Ionospheric measurements were collected from 10 HF transmitters, five HF receivers, and four ionosondes strategically located throughout WSMR as depicted in Figure 8. Despite the availability of five HF receivers, this project only focuses on data collected at the G10 receiver. The AoA circuit midpoint is the geographical halfway distance between the transmitter and G10 receiver, for which the reflection point is defined. The distance between each AoA circuit midpoint and ionosonde is found in Table 2.

As previously mentioned, the DPS4 and DPS4D were the ionosonde in use at WSMR. The four ionosondes located at Kirtland, Munyo, Cherry, and Squirt, transmitted a beam vertically upward across a range of frequencies and measured the time delay for the signal to be returned in order to calculate the altitude at which the radio wave was reflected. Each of the ionosondes measured the ionosphere at a different cadence; observations at Cherry occurred every 2 minutes, while Kirtland, Munyo, and Squirt were predominately every 6 minutes, with occasional periods at 2 minutes.

AoA measurements were collected for each of the HF transmitters to G10 receiver.

Table 2. Distance (km) between ionosonde and transmitter to G10 receiver midpoint.

	RDS1	RDS2	ROB	POL	FRN	OSC	PND	QEN	GRN	N1
Cherry	9.4	9.4	11.3	5.7	11.6	15.7	13.8	13.8	24.8	23.9
Squirt	46.6	46.6	61.4	58.7	65.9	63.6	68.3	68.4	79.3	78.0
Munyo	84.7	84.7	70.5	73.4	65.4	72.2	63.0	63.3	52.0	55.0
Kirtland	242.6	242.6	229.5	229.2	223.3	224.6	220.6	219.8	210.3	210.0
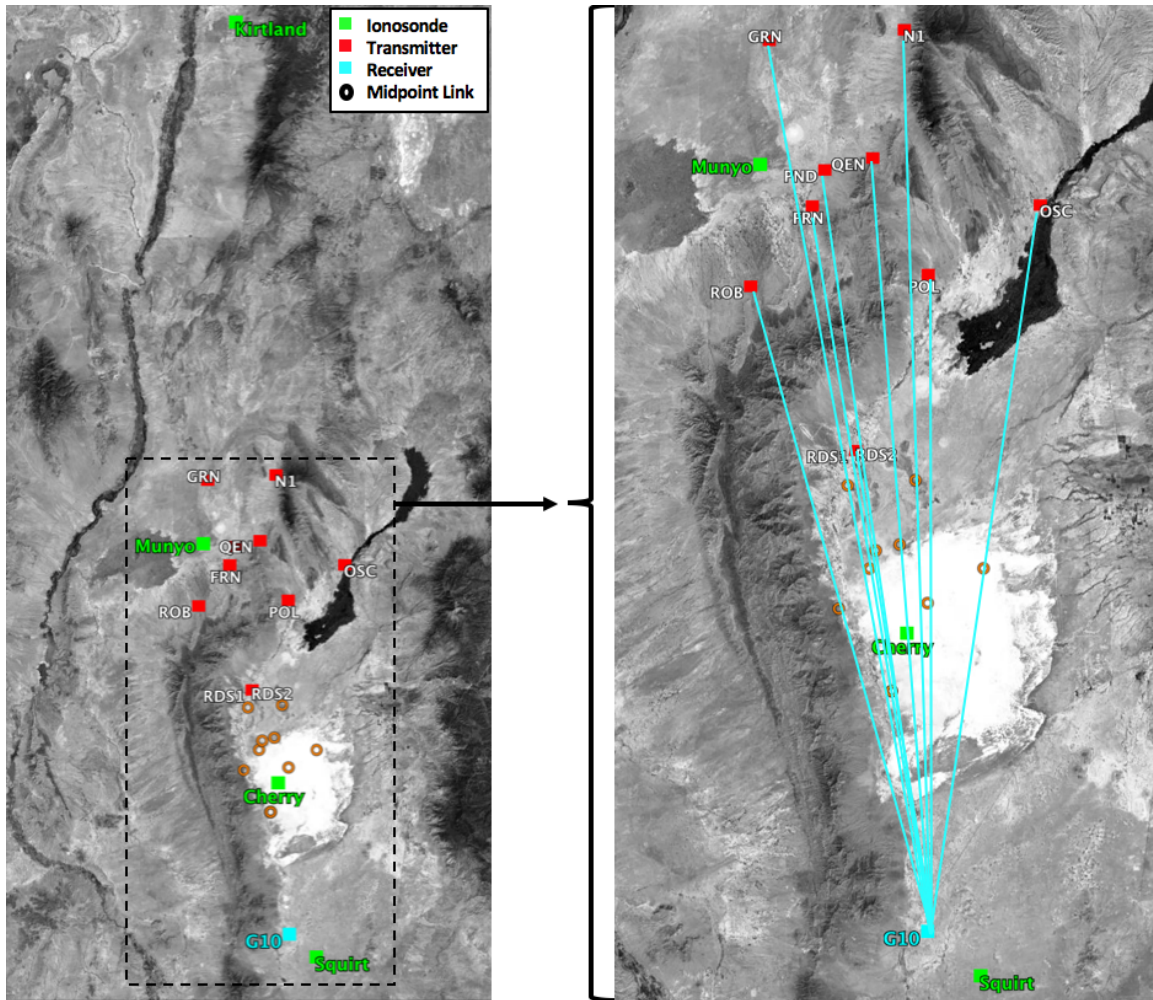
Figure 8. Map of WSMR sensors during January 2014 IARPA HFGeo field campaign.

AoA measurements provide azimuth and elevation angles of the radio wave incident upon the receiver following sky wave propagation (Figure 6). Measurements for both AoA angles are available; however, this project only analyzes the AoA elevation angle. AoA measurements were recorded on average approximately every 3 to 5 seconds.

Availability of AoA data is limited to eight of the 14 day field campaign. Using ionosonde measurements from Cherry, each of the eight day's data sets are characterized as either a quiet period in which the ionosphere remains relatively stable, or a TID period based on ionosonde measurements from Cherry. To ensure diurnal

variations in the electron density profile do not distort observations, ionograms from Cherry are examined for a hook signature in the O-mode profile (Figure 2) between 1800-2400 UT. From this evaluation, there were no hooks in the Cherry ionogram O-mode profile between 2100-2300 UT on 21 January 2014, so this period is defined as the quiet period. However, there is a well defined hook in the O-mode profile on the Cherry ionogram at 1934 UT on 26 January 2014; therefore, to capture the extent of the TID before and after it propagates through Cherry, the TID period is defined as 1900-2200 UT.

During the quiet and TID period, AoA data is limited to a few frequencies. Ionosondes transmit across a range of frequencies, so the frequency selected for the quiet and TID periods is based on the frequency of the AoA measurements. To ensure an accurate comparison of AoA and ionosonde measurements, both data sets are analyzed at the same frequency for the respective day. The quiet period frequency is 5.3 MHz, and the TID period frequency is 5.34 MHz.

Using AoA and ionosonde data from this field campaign, the following are determined in the next sections: correlation between AoA elevation angle and ionosonde virtual height measurements, TID wave characteristics as extracted from a spectral analysis, the TID velocity, temporal cross-correlation estimates of the time a TID impacts an AoA circuit midpoint and how the wave structure changes over distance, and lastly, a simple model to predict a change in AoA elevation angles.

20

3.2. Elevation Angle and Virtual Height Correlation

Data collected during the quiet and TID periods are analyzed to determine the correlation between AoA elevation angle and ionosonde virtual height measurements. Given that AoA measurements are in degrees and the ionosonde measurements in kilometers, the MM method is applied to the AoA data to provide a height-to-height comparison. The reliability of the MM method is assessed by analyzing both the quiet and TID period to determine if heights from the AoA MM method are comparable with the ionosonde virtual height measurements. To ensure consistency when analyzing the two periods, AoA measurements from the G10-RDS1 circuit and ionosonde measurements from Cherry are evaluated. G10-RDS1 is selected because it is the nearest midpoint link to Cherry with data available during both periods.

Recall from Chapter II that the MM method treats the ionospheric reflection point as a horizontal mirror. Therefore, if the distance between the transmitter and receiver, d, and the AoA elevation angle, ϵ, are known, the height at the reflection point, h, is

$$h = \frac{d}{2\tan(\epsilon)} \tag{7}$$

The distance variable, d, is calculated by setting the shape of the Earth as an ellipsoid, then transforming the latitude and longitude coordinates from geodetic to Cartesian. Once the transmitter and receiver are in Cartesian coordinates, the distance variable is solved through the Pythagorean theorem. To solving for the height at the reflection point, the AoA elevation angle must be converted from degrees to radians.

Application of the MM is shown in Figure 9 as the G10-RDS1 AoA MM heights, and the Cherry ionosonde virtual heights are plotted against time for the quiet period. This image shows the AoA MM heights fluctuating more with time than the ionosonde

21
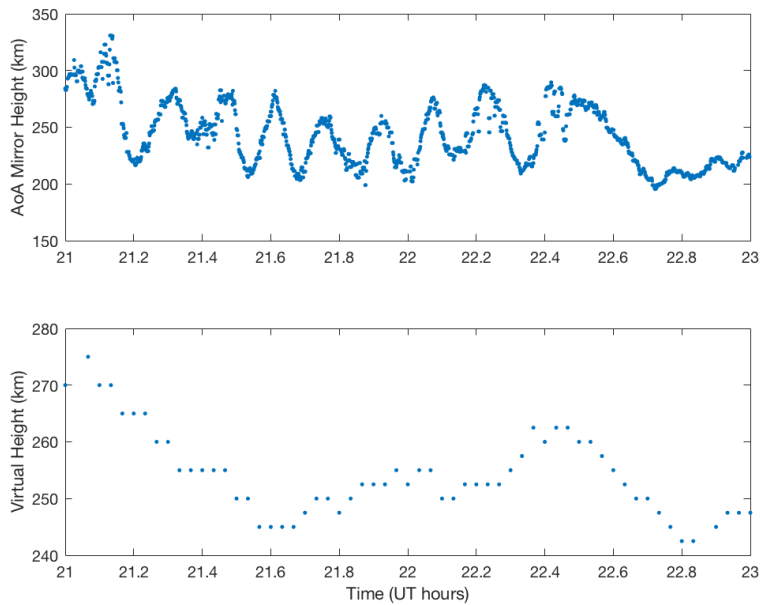
Figure 9. Quiet period measurements for G10-RDS1 and Cherry using the 5.3 MHz frequency on 21 Jan 2014, from 2100-2300 UT. Top: AoA MM height versus time at G10-RDS1. Bottom: Cherry ionosonde virtual height measurements versus time. Despite different measurements and cadence, both AoA MM heights and ionosonde virtual heights have a mean height of 254 km.

virtual heights; this may be due to the cadence at which AoA and ionosonde measurements are taken. Despite the two plots not matching exactly, the MM appears relatively close as both data sets have a mean height of 254 km. A second analysis during the quiet period is shown in Figure 10 with AoA MM heights at G10-FRN and ionosonde virtual heights at Cherry. Similar to the first comparison, the AoA MM heights at G10-FRN oscillate more than the ionosonde virtual heights; however, the mean AoA MM height is 244 km, only 10 km from that at Cherry. Additionally, both figures show AoA MM heights that fluctuations as much as 100 km, revealing that despite the name, the quiet period is anything but quiet, as the ionosphere does not remain perfectly flat.

The MM method performs well during the quiet period, but breaks down during the TID period (Figure 11). The AoA MM heights for G10-RDS1 are nearly 1.5 to

22
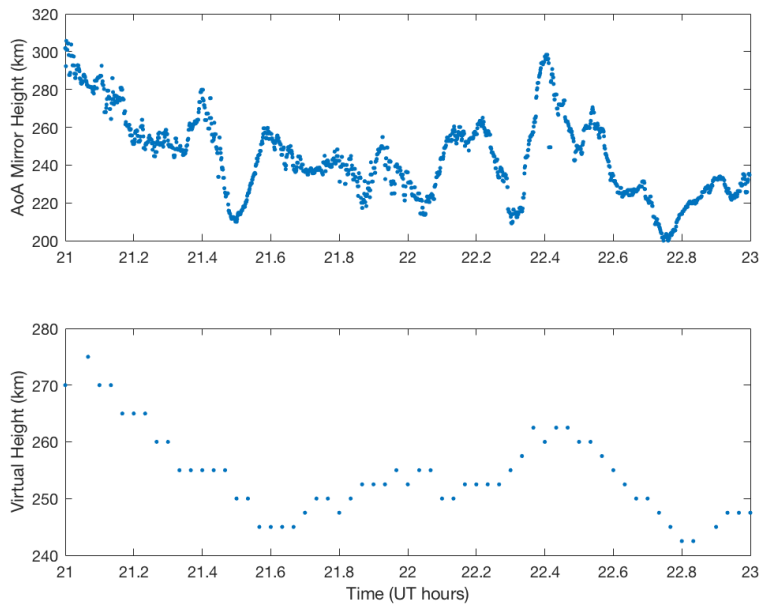
Figure 10. Quiet period measurements for G10-FRN and Cherry using the 5.3 MHz frequency on 21 Jan 2014, from 2100-2300 UT. Top: AoA MM model height versus time for G10-FRN, with a mean height of 244 km. Bottom: Cherry ionosonde virtual height measurements versus time, with a mean height of 254km.

2.3 times greater than ionosonde virtual heights at Cherry on 26 January 2014, from 1900-2200 UT during a TID. Similarly, Figure 12 shows MM heights at G10-POL that are 1.2 to 1.9 times greater than virtual heights at Cherry during this same period. Additionally, AoA MM heights of nearly 600 to 700 km are predicted, which are well above the F2 peak. These MM heights are too high because the MM does not account for the tilt at the reflection point. Therefore, given that the AoA MM heights deviate too far from ionosonde virtual heights, the MM method is not recommended during a TID without taking tilts into consideration.

Given the MM method does not handle the TID period well, the next approach is to evaluate the AoA elevation angle. While, this analysis does not provide a simple height-to-height comparison, it allows for a comparison with no conversion required. Correlation values include the Pearson correlation coefficient (r) and a p-value to

www.manaraa.com

Figure 11. TID period measurements of the 5.34 MHz frequency on 26 Jan 2014, from 1900-2200 UT. Top: G10-RDS1 AoA MM height versus time. Bottom: Cherry ionosonde virtual height measurements versus time. Note the AoA MM heights are 1.5 to 2.3 times greater than Cherry ionosonde virtual heights.

indicate the confidence in fit.

As mentioned in Section 3.1, there is a time disparity between the cadence of AoA and ionosonde measurements that must be accounted for prior to computing the correlation. This disparity is shown in Figures 13, as AoA measurements from G10-RDS1 occur every few seconds while Cherry ionosonde measurements happen every 2 minutes. Therefore, a 1 minute time constraint is placed on the amount of separation that is allowed to exist between the AoA and ionosonde measurements. This same time constraint is used throughout the remainder of this research project anytime a correlation comparison is performed.

Figure 13 displays the G10-RDS1 AoA elevation angle and the Cherry ionosonde virtual height measurements during the quiet period. Using the time constraint described above, a correlation of these two data sets yields a moderately positive Pearson

24

Figure 12. TID period measurements of the 5.34 MHz frequency on 26 Jan 2014, from 1900-2200 UT. Top: G10-POL AoA MM height versus time. Bottom: Cherry ionosonde virtual heights versus time. Note the AoA MM heights are 1.2 to 1.9 times greater than ionosonde virtual heights.

correlation coefficient of r=0.58 and a p-value of 0.00, as is shown in Figure 14. A second analysis during the quiet period is provided in Figure 15 for the G10-FRN AoA and Cherry ionosonde measurements. The G10-FRN elevation angles oscillate through a range of nearly 5°, while virtual height measurements at Cherry oscillate approximately 50 km. The correlation of the two data sets is shown in Figure 16 and indicates that G10-FRN AoA elevation angles have a strong positive correlation with Cherry ionosonde virtual heights, with r=0.64. Since both G10-RDS1 and G10-FRN elevation angles are positively correlated with virtual height measurements at Cherry during the quiet period, the next step is to analyze correlation during the TID period.

An overview of the TID period is displayed in Figure 17, with AoA elevation angles and ionosonde virtual heights provided for each of the sites. The dynamics of the ionosphere during the TID period reveal AoA elevation angle measurements

25

Figure 13. Quiet period measurements of the 5.3 MHz frequency on 21 Jan 2014, from 2100-2300 UT. Top: AoA elevation angle versus time at G10-RDS1. Bottom: Cherry ionosonde virtual height measurements versus time.

Figure 14. Quiet period scatter plot of Figure 13. Correlation is measured between G10-RDS1 AoA elevation angle and Cherry ionosonde virtual height measurements. The correlation values are: r=0.58 and p-value=0.00.

26

Figure 15. Quiet period measurements of the 5.3 MHz frequency on 21 Jan 2014, from 2100-2300 UT. Top: AoA elevation angle versus time at G10-FRN. Bottom: Cherry ionosonde virtual height measurements versus time.

Figure 16. Quiet period scatter plot of Figure 15. Correlation is measured between G10-FRN AoA elevation angle and Cherry ionosonde virtual height measurements. The correlation values are: r=0.64 and p-value=0.00.

27
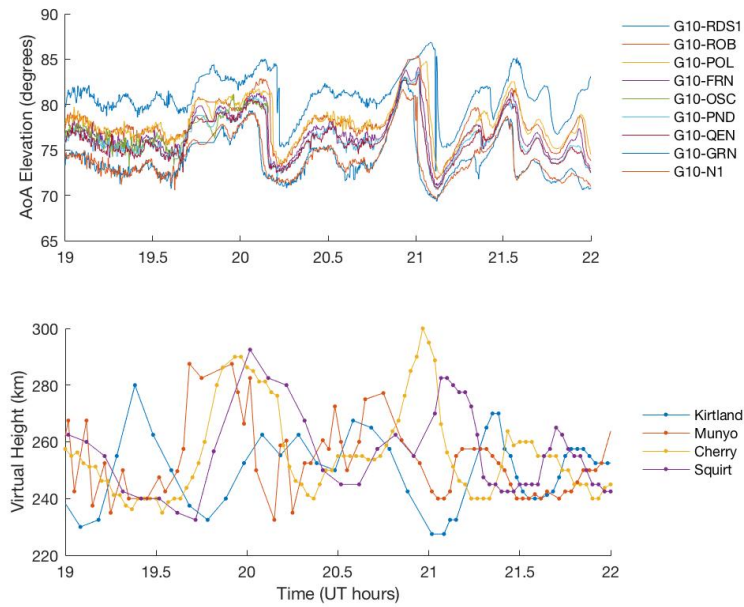
Figure 17. Measurements of the 5.34 MHz frequency on 26 Jan 2014, from 1900-2200 UT during the TID period. The top plot shows AoA elevation angle measurements versus time for each of the transmitters to G10 receiver. The trend of these measurements are similar as the circuits are at most separated by 33 km. The bottom plot shows virtual height measurements versus time for each of the four ionosondes. The Cherry ionosonde most closely resembles the AoA measurements, while Kirtland ionosonde is the most out of phase with AoA measurements.

follow a similar trend over time as the wave propagates south; however, the same cannot be said for the ionosonde measurements. The Cherry ionosonde virtual height measurements most closely resembles the trend of the AoA elevation angles, because of the close proximity to the circuit midpoints. However, a comparison of the AoA elevation angle and ionosonde virtual heights show a reduction in correlation as the distance between AoA circuit midpoint and ionosonde is increased. The first comparison is for the nearest AoA midpoint link and ionosonde, G10-POL and Cherry, with a separation distance of 6 km. Figure 18 shows a similar trend for the G10-POL AoA elevation angle and Cherry virtual heights, as both data sets begin to increase shortly after 1930 UT when the TID is first measured, and then oscillate together for the remaining 2.5 hours. The correlation of the two sets indicate a strong positive

28
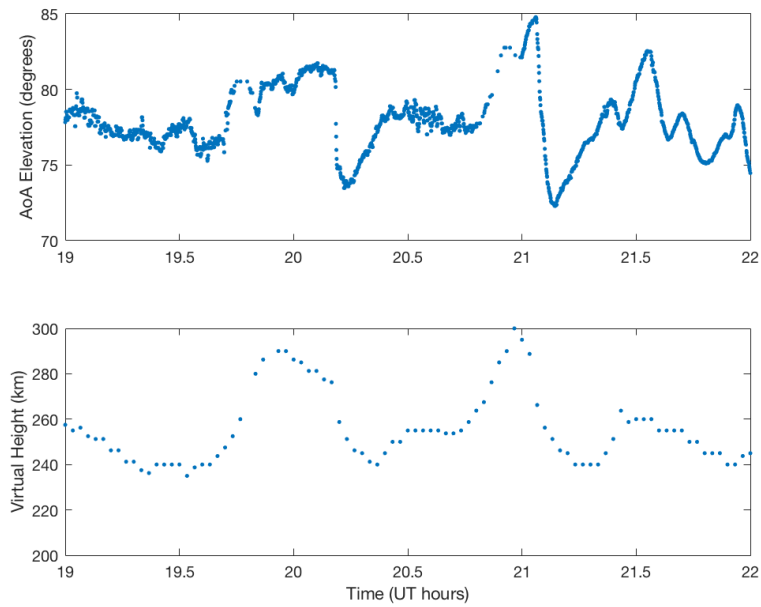
Figure 18. TID period measurements of the 5.34 MHz frequency on 26 Jan 2014, from 1900-2200 UT. Top: AoA elevation angle versus time at G10-POL. Bottom: Cherry ionosonde virtual height measurements versus time.

correlation with r=0.72 (Figure 19).

A second analysis during the TID is performed between G10-RDS1 and Cherry, which extends the distance between AoA and ionosonde from 6 to 9 km. G10-RDS1 AoA elevation angles and Cherry ionosonde virtual heights follow the same trend (Figure 20) with a strong correlation of r=0.61, as noted in Figure 21. The close proximity of the Cherry ionosonde with each of the AoA midpoint links yields a strong positive correlation.

To analyze the change in correlation as the distance between the AoA midpoint and ionosonde increases, G10-RDS1 AoA measurements are compared to the further ionosondes. Changing the ionosonde from Cherry to Squirt increases the AoA midpoint to ionosonde distance from 9 to 47 km. Figure 22 shows the AoA elevation measurements for G10-RDS1 and virtual heights from Squirt. The Squirt virtual height measurements are out of phase with the AoA elevation angle, providing virtu-

29
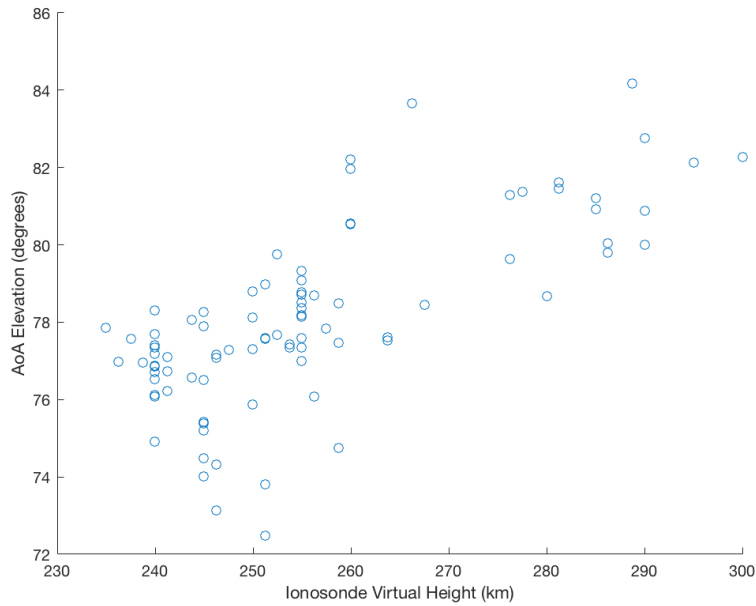
Figure 19. TID period scatter plot of Figure 18, G10-POL AoA elevation angle and Cherry ionosonde virtual height measurements during a TID. The correlation values are: r=0.72 and p-value=0.00.
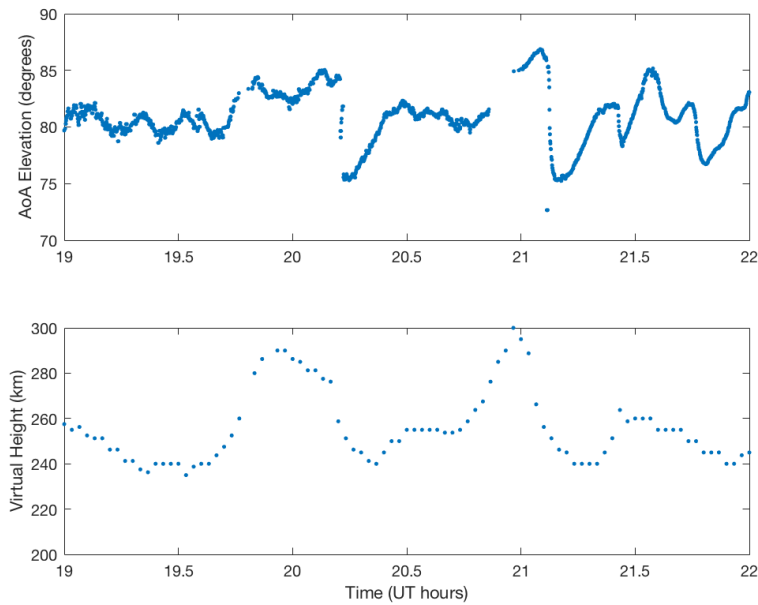
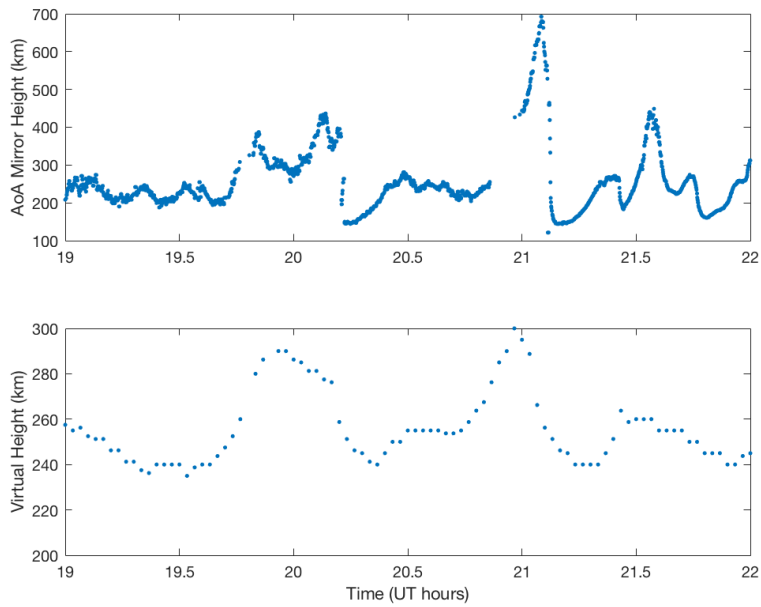**Figure 20. TID period measurements of the 5.34 MHz frequency on 26 Jan 2014, from 1900-2200 UT. Top: G10-RDS1 AoA elevation angle versus time. Bottom: Cherry ionosonde virtual height measurements versus time.**

30
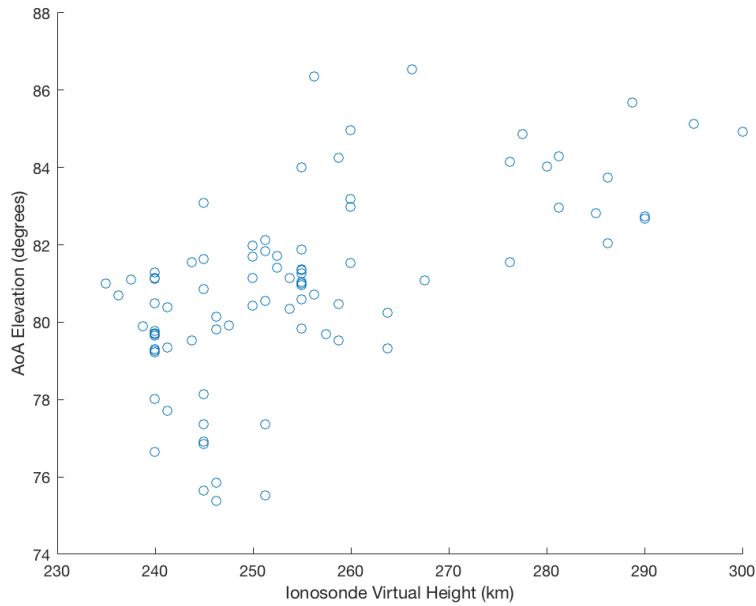
Figure 21. TID period scatter plot of Figure 20, G10-RDS1 AoA elevation angle and Cherry ionosonde virtual height measurements during a TID. The correlation values are: r=0.61 and p-value=0.00.
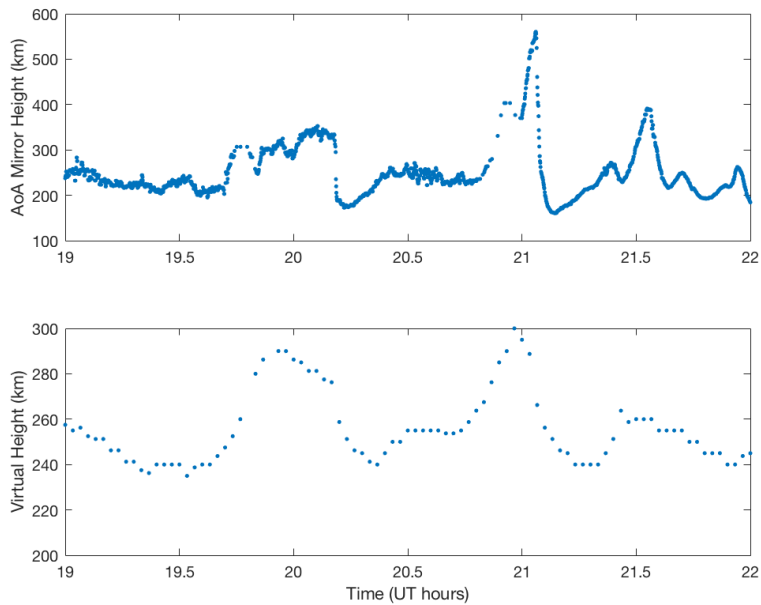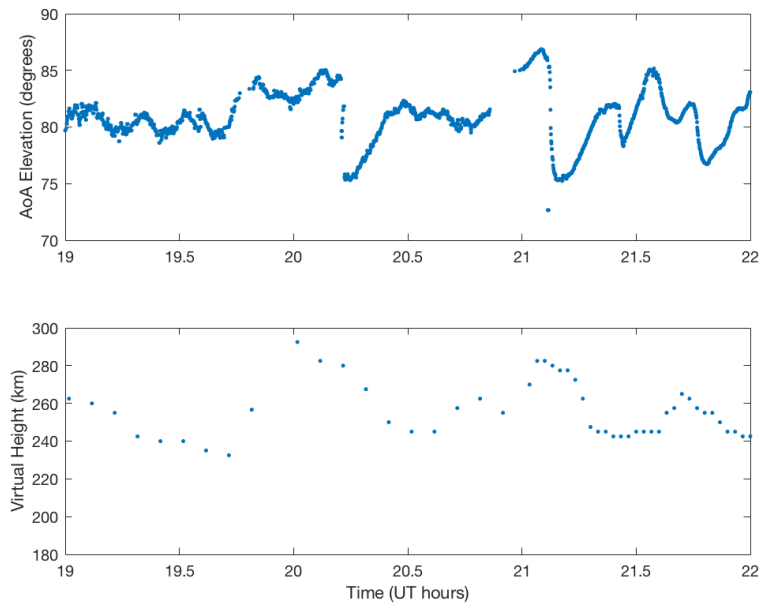

Figure 22. TID period measurements of the 5.34 MHz frequency on 26 Jan 2014, from 1900-2200 UT. Top: G10-RDS1 AoA elevation angle versus time. Bottom: Squirt ionosonde virtual height measurements versus time.

31

ally no correlation with r=0.03 (Figure 23).

Using the Munyo ionosonde, the comparison in Figure 24 displays the measurements for G10-RDS1 AoA elevation angles and Munyo virtual heights. Similar to Squirt, virtual heights at Munyo are occasionally out of phase providing r=0.03 (Figure 25). In this instance, the Pearson correlation coefficient is the same as measured for Squirt, despite the virtual height measurements being different. The last correlation comparison is between G10-RDS1 and Kirtland, where the separation distance is 233 km. Figure 26 shows the Kirtland virtual height measurements are out of phase with G10-RDS1 AoA elevation angles, which is highlighted by the negative correlation, r=-0.13, in Figure 27. This trend suggests that as the distance between the AoA midpoint link and ionosonde increases, the correlation decreases.

An e-folding distance for the correlation between AoA elevation angle and ionosonde virtual height as a function of distance is calculated by including additional AoA links.
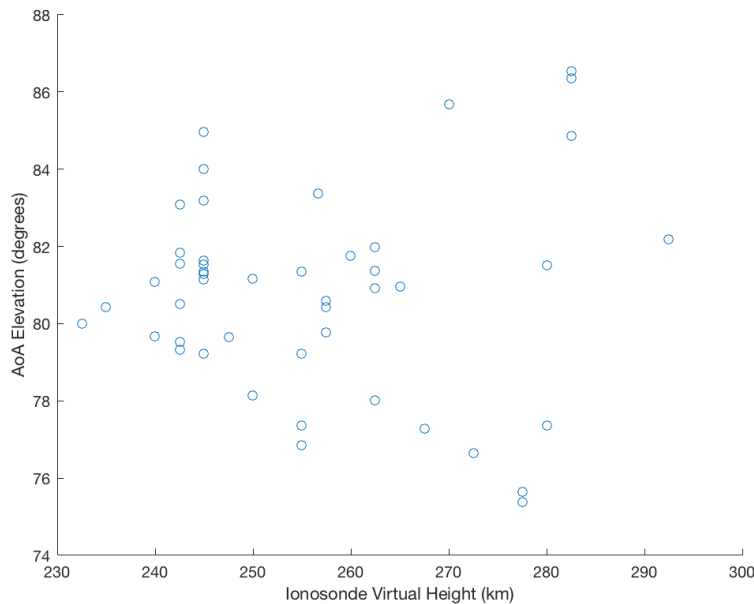
Figure 23. TID period scatter plot of Figure 22, G10-RDS1 AoA elevation angle and Squirt ionosonde virtual height measurements during a TID. The correlation values are: r=0.03 and p-value=0.84.
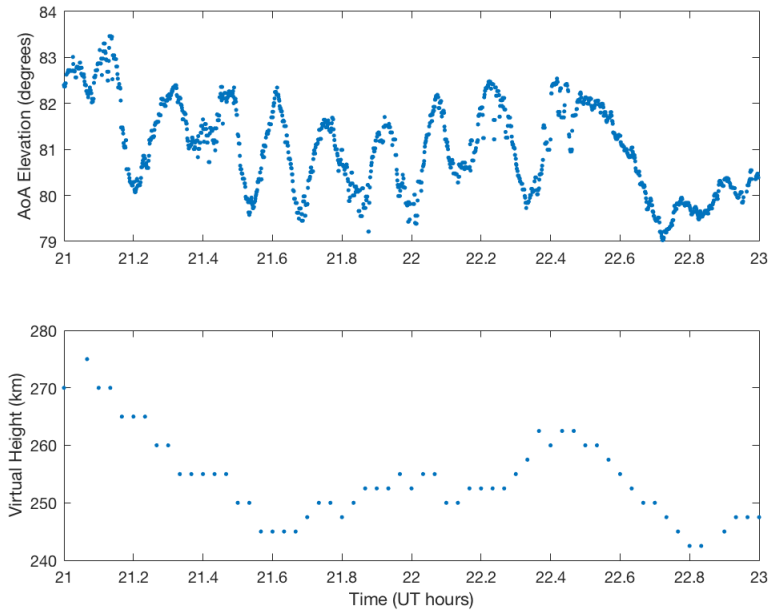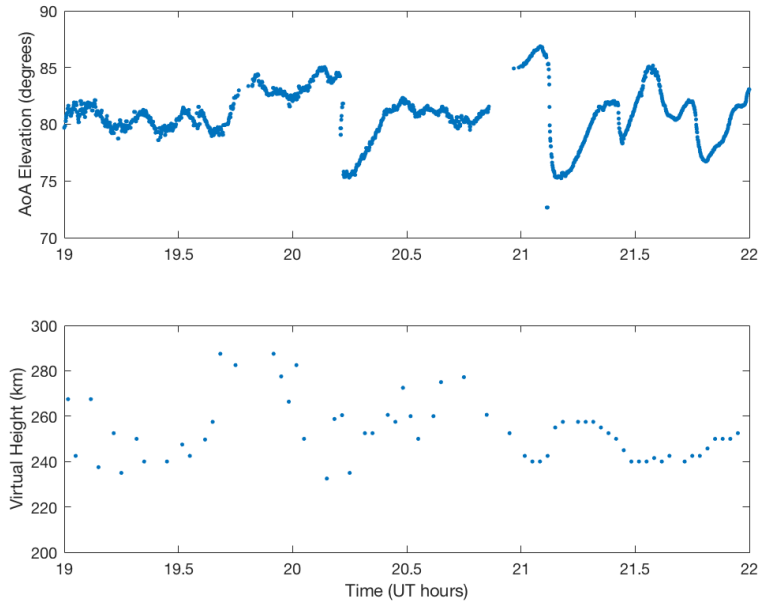
Figure 24. TID period measurements of the 5.34 MHz frequency on 26 Jan 2014, from 1900-2200 UT. Top: G10-RDS1 AoA elevation angle versus time. Bottom: Munyo ionosonde virtual height measurements versus time.
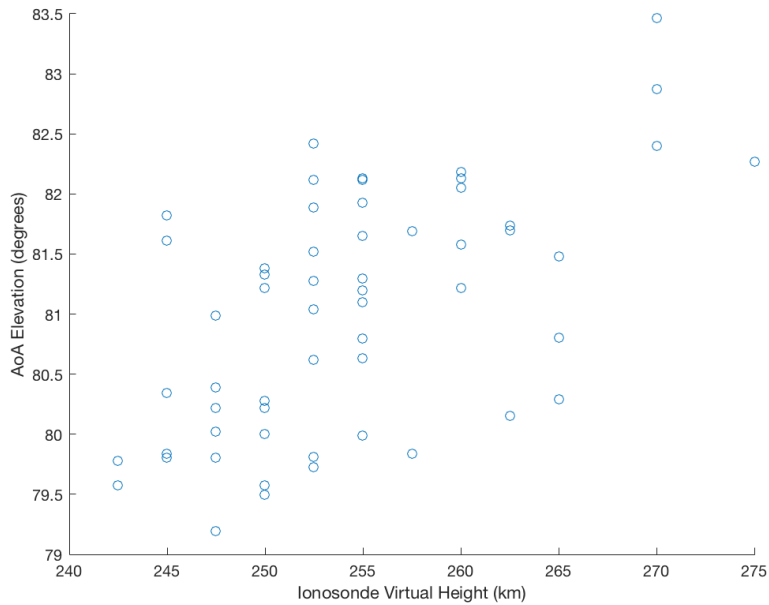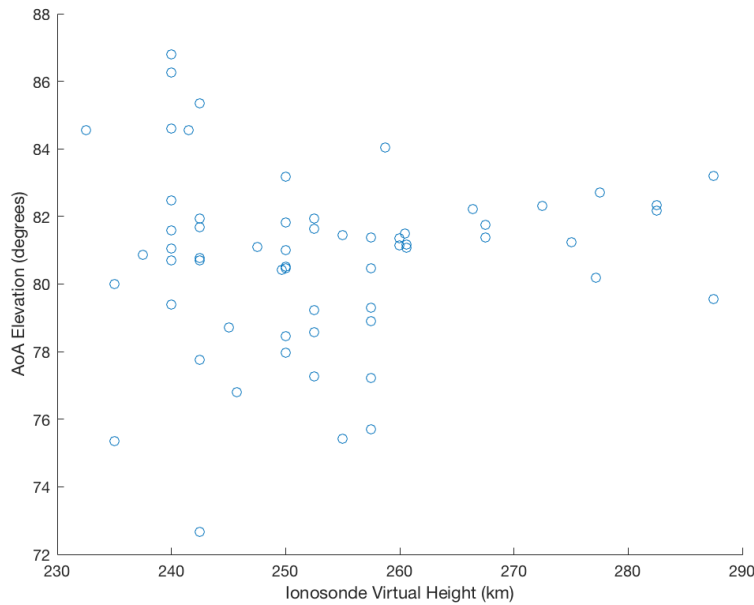

Figure 25. TID period scatter plot of Figure 24, G10-RDS1 AoA elevation angle and Munyo ionosonde virtual height measurements during a TID. The correlation values are: r=0.03 and p-value=0.80.
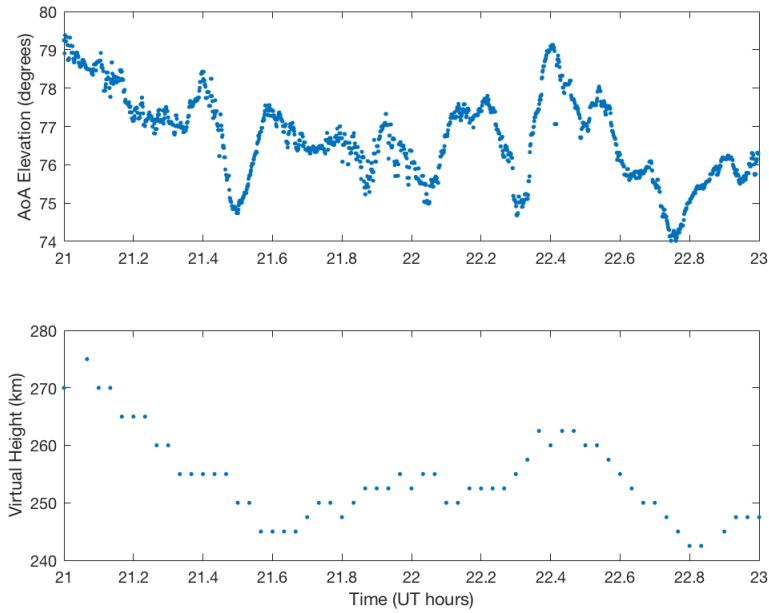
33
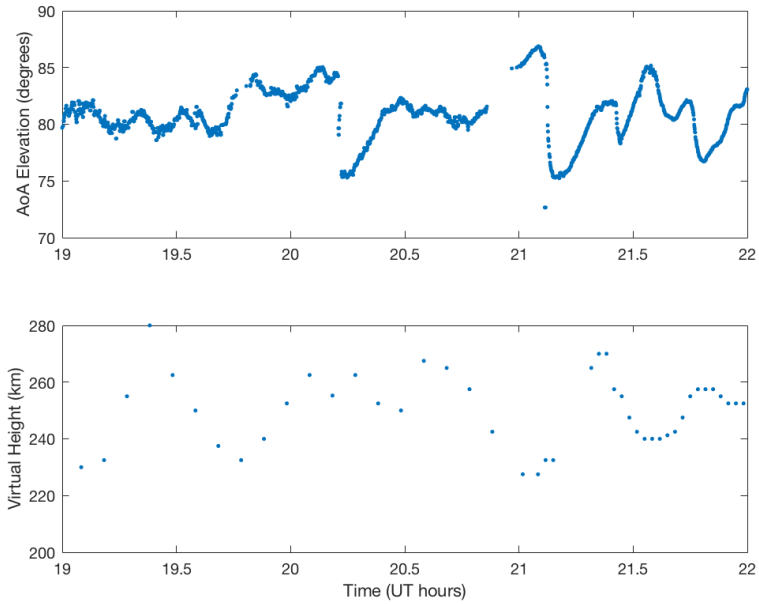
Figure 26. TID period measurements of the 5.34 MHz frequency on 26 Jan 2014, from 1900-2200 UT. Top: G10-RDS1 AoA elevation angle versus time. Bottom: Kirtland ionosonde virtual height measurements versus time.
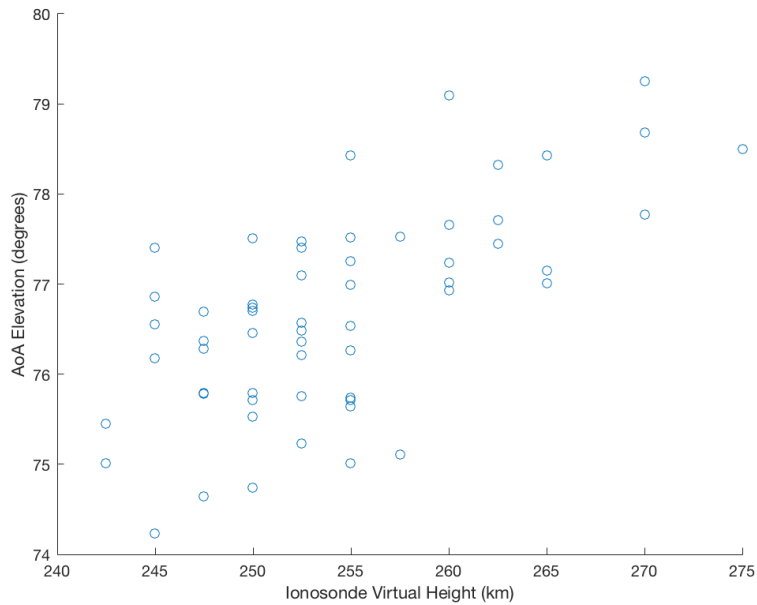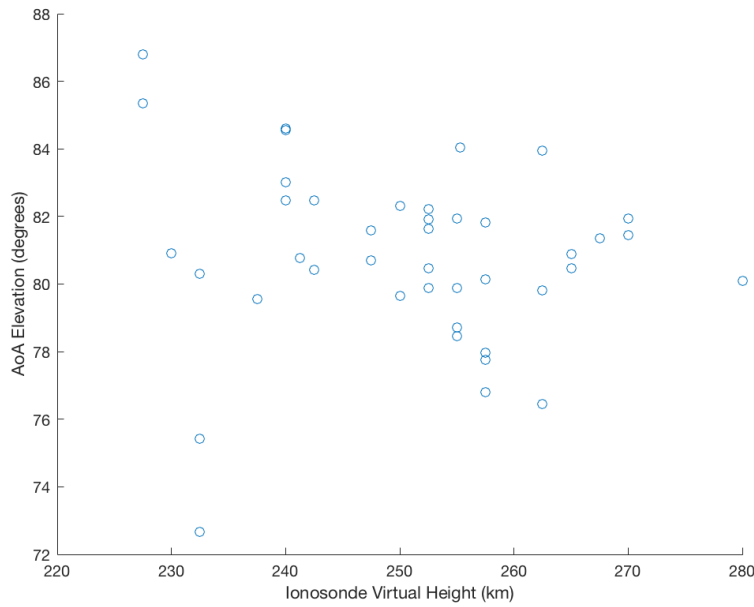

Figure 27. TID period scatter plot of Figure 26, G10-RDS1 AoA elevation angle and Kirtland ionosonde virtual height measurements during a TID. The correlation values are: r=-0.13 and p-value=0.40.

34

The distance between the four ionosondes and each of the AoA midpoint links is illustrated in Figure 28. AoA midpoint links are closest to Cherry at less than 25 km, slightly further from Munyo and Squirt at distances between 45 to 90 km, and furthest from Kirtland at distances greater than 200 km. The correlation between each AoA midpoint link and ionosonde is displayed in Figure 29 (except RDS2 and OSC due to insufficient data). The e-folding distance is calculated by applying a non-linear fit to the correlation data. The non-linear fit reveals an e-folding distance of 37 km, with an error of ± 5 km at one standard deviation, which indicates that the correlation varies with distance as $r \sim \exp(-x/37)$, where x is the distance (km) between the AoA circuit midpoint and ionosonde.

Additionally, Figure 29 indicates the distance at which AoA elevation angle and ionosonde virtual height measurements are in phase. Based on the strong correlation values reported at Cherry, it is assumed that when measurements are taken at less
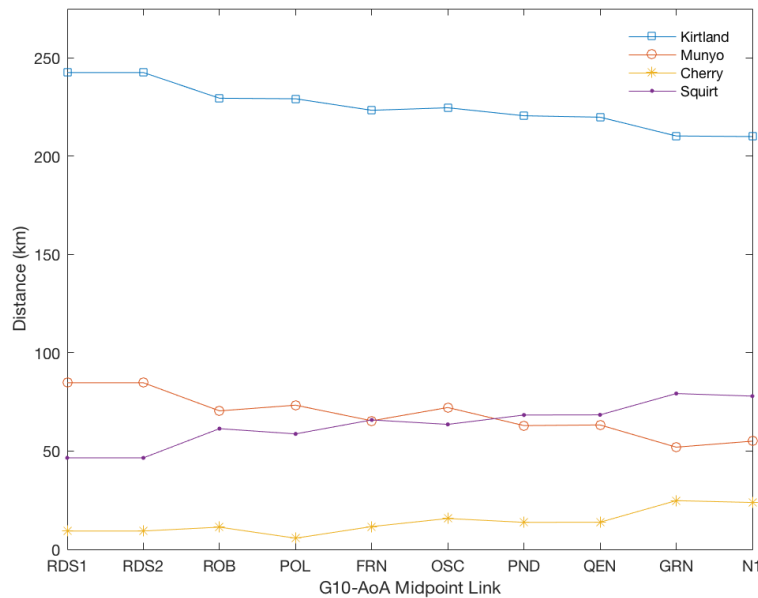
Figure 28. Distance between ionosonde and G10 receiver to respective transmitter midpoint link.
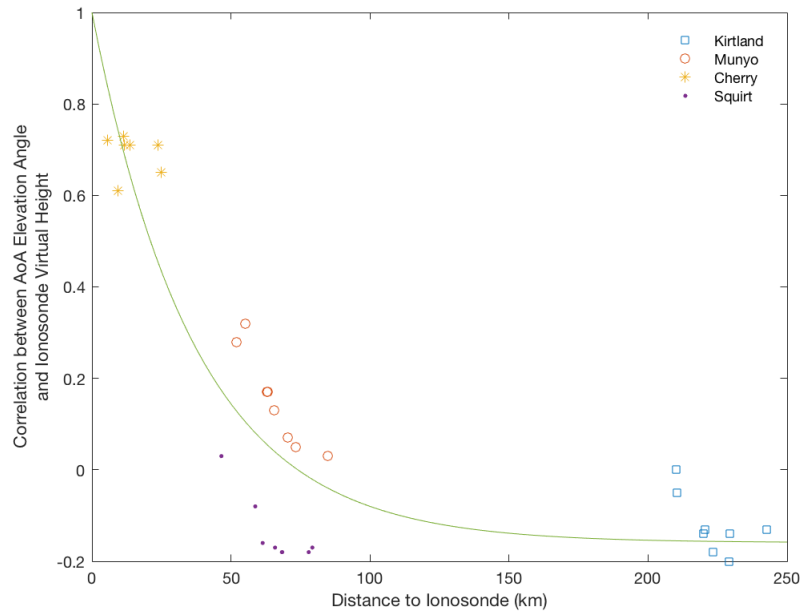
Figure 29. AoA elevation angle and virtual height correlation as a function of distance during the TID period. The correlation, r, decreases exponentially as the distance between AoA midpoint link and ionosonde increases, following $r \sim \exp(-x/37)$, where x is distance (km).

than 25 km, the two waves will be in phase. However, as the distance increases beyond 50 km, the correlation will be weak at best, and more than likely found to have no correlation because the waves are out of phase.

3.3. Spectral Analysis

A correlation of AoA elevation angles and ionosonde virtual heights suggests that the correlation versus distance drops off exponentially with an e-folding distance of 37 km during the TID period; however, this reveals nothing about the characteristics of the TID. Information on the wave structure of the TID can be determined with spectral analysis on the AoA elevation angles and ionosonde virtual heights. The spectral analysis applies a discrete Fourier transform (DFT), by which the amplitude and phase of the waves comprising the TID are extracted.

Figure 30 shows measurements for G10-N1 AoA elevation angles and Kirtland ionosonde virtual heights during the TID period, revealing the inconsistent measurements throughout the span of ionosonde virtual height plot, as well as the gaps in AoA elevation angles near 1945 UT and 2100 UT. Therefore, to ensure the wave is continuous with constant time steps, a cubic spline interpolation function is applied
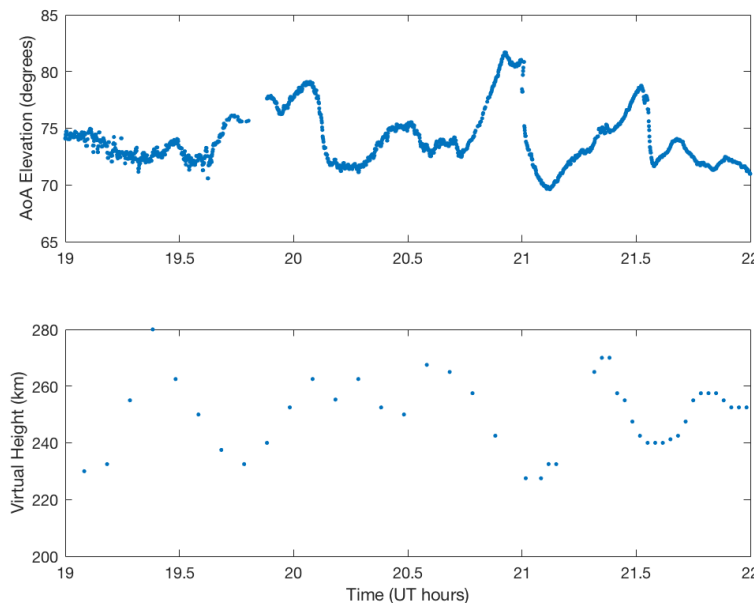
Figure 30. Measurements of G10-N1 AoA elevation angle and Kirtland ionosonde virtual height for 5.34 MHz frequency on 26 Jan 2014 from 1900-2200 UT.

to both data sets. This function fills in the data gaps to provide a wave with a continuous second-order derivative, as well as continuous third-order derivatives for the first and last end points [MathWorks, 2017]. Once the cubic spline interpolation function is applied, Figure 31 reveals the new continuous wave, where red asterisks represent the actual data measurements and blue triangles are the interpolated data points. From this continuous function, a DFT of the wave is performed to complete the spectral analysis during the TID period.

The spectral analysis for both G10-N1 AoA elevation angles and Kirtland ionosonde virtual heights are shown in Figure 32. A strong amplitude of the wave, as measured by the AoA elevation angle, is found at a period of 30 minutes. However, data from the Kirtland ionosonde, 210 km north of the G10-N1 midpoint link, reveals the peak amplitude of the wave for a period of 36 minutes. Additionally, Figure 32 displays the
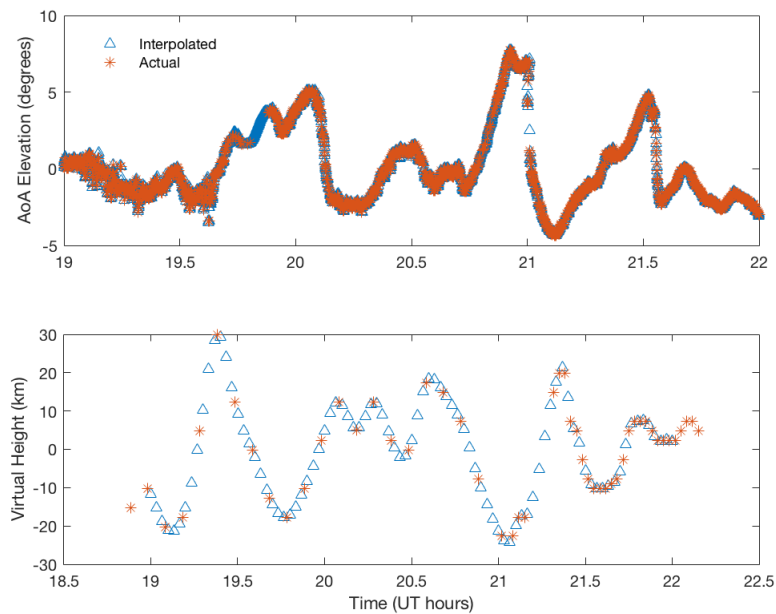
Figure 31. Cubic spline interpolation of the G10-N1 AoA elevation angle and Kirtland ionosonde virtual height measurements displayed in Figure 30. The red asterisks represent actual data measurements and the blue triangles are the interpolated data points from the cubic spline interpolation function.
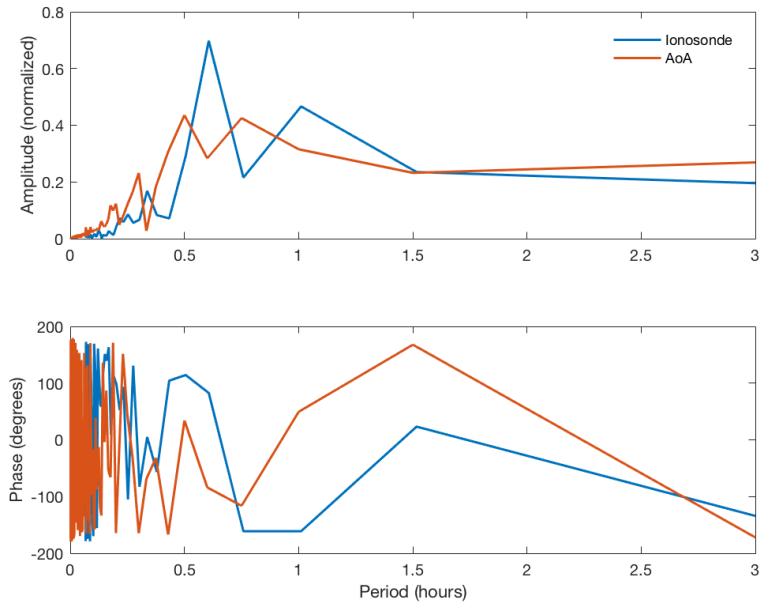
Figure 32. DFT of the interpolated G10-N1 AoA elevation angle and Kirtland ionosonde virtual height measurements displayed in Figure 31. The peak wave amplitude of the TID at G10-N1 occurs at a 30 minute period, and at Kirtland occurs at 45 minute period.

phase of the wave as a function of period for both data sets. This phase information is used to calculate the TID velocity and will be discussed in the next section.

A plot of the DFT for each site shows how the TID changes as the wave propagates from north to south. Figure 33 shows the DFT of the G10-QEN AoA elevation angles and Munyo ionosonde virtual heights. Analysis of this figure reveals the peak amplitude of the wave at G10-QEN occurs at a period of 30 minutes. At Munyo, where the wave is 160 km south of Kirtland, the peak amplitude has a 45 minute period. Figure 34 displays the DFT further south for G10-POL and Cherry. The peak wave amplitude of the TID at G10-POL is at a 30 minute period. Examination of the wave over Cherry, 233 km south of Kirtland, shows a peak amplitude at a 1 hour period. Finally, a DFT for the two southern most sites, G10-RDS1 and Squirt, is shown in Figure 35. The peak wave amplitude of the TID measured over G10-RDS1

www.manaraa.com
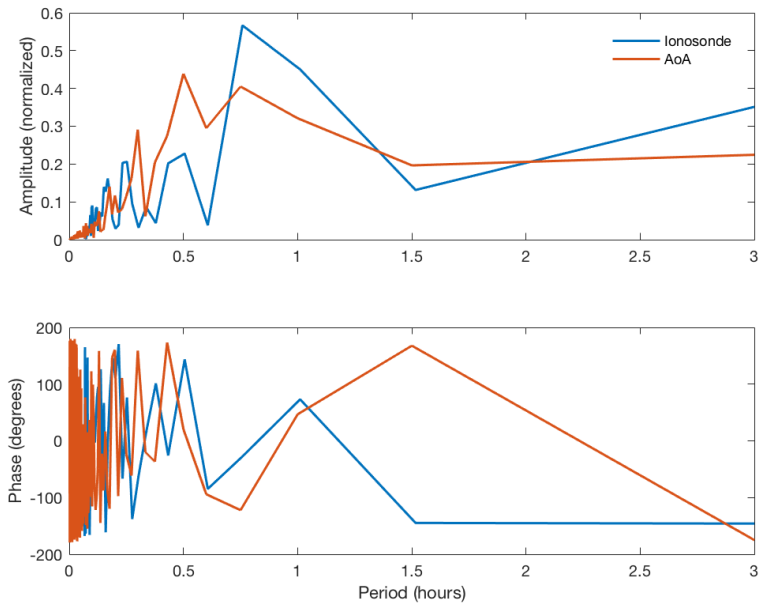
Figure 33. DFT of G10-QEN AoA and Munyo ionosonde measurements. The peak wave amplitude of the TID at G10-QEN AoA occurs at a 30 minute period, and at Munyo occurs at a 45 minute period.
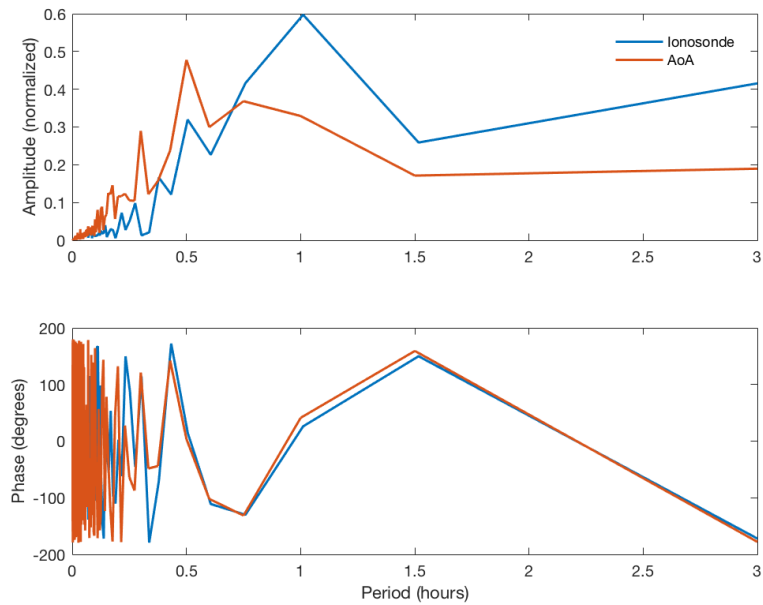
Figure 34. DFT of G10-POL AoA and Cherry ionosonde measurements. The peak wave amplitude of the TID at G10-POL AoA occurs at a 30 minute period, and at Cherry occurs at a 1 hour period.

40
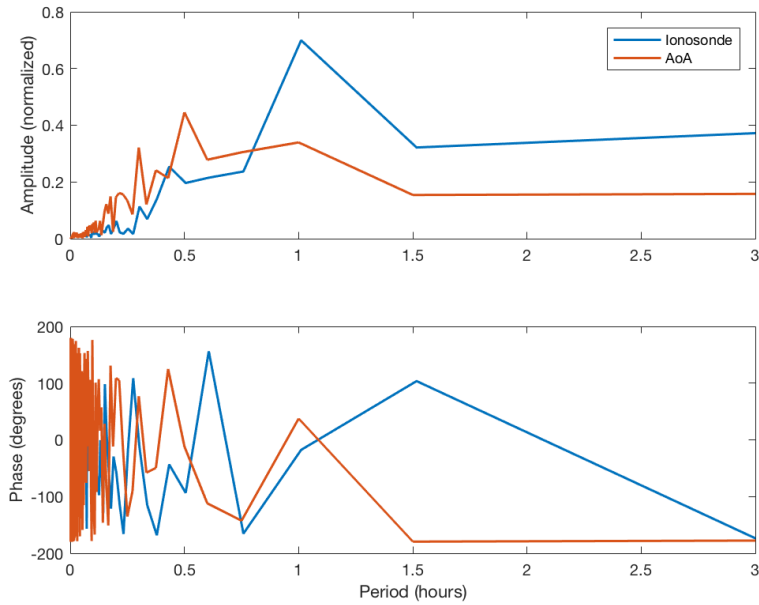
Figure 35. DFT of G10-RDS1 AoA and Squirt ionosonde measurements. The peak wave amplitude of the TID at G10-RDS1 AoA occurs at a 30 minute period, and at Squirt occurs at a 1 hour period.

is found at a 30 minute period, and at Squirt, 288 km south of Kirtland, the peak amplitude is at a one hour period.

The DFTs in Figures 32 to 35 show little variation in the AoA elevation angles, but reveal much larger fluctuations in the spectrum of ionosonde virtual heights. Evaluation of the AoA elevation angles as the TID travels 33 km from the northern (G10-N1) to southern (G10-RDS1) most sites maintaining a peak 30 minute period. However, larger variation in the spectrum of ionosonde virtual heights are shown in Figure 36 indicating the dominant TID peak amplitude varies as the wave propagates from north to south over a distance of 288 km. The dominant TID amplitude occurs with a period of 36 minutes at Kirtland, 45 minutes at Munyo, and 1 hour at Cherry and Squirt. From the AoA and ionosonde spectral analysis, TID characteristics change very little over short distances; however, at greater distances as observed by the ionosondes, the TID characteristics change as the wave propagates south.

41

Thus, the TID that is observed at Kirtland will not possess the same characteristics as the TID measured at Squirt.
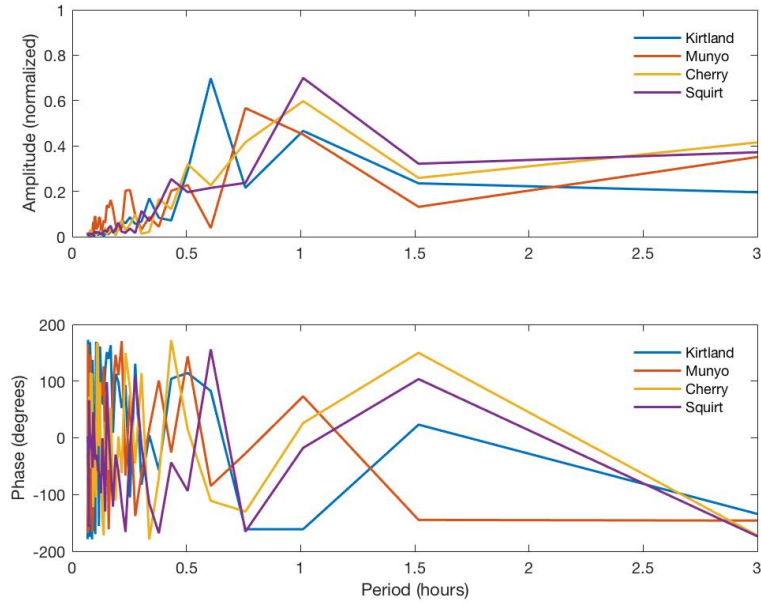
Figure 36. DFT of the 5.34 MHz frequency from the ionosondes at WSMR on 26 Jan 2014 from 1900-2200 UT. This reveals how the amplitude and phase change as the TID propagates south from Kirtland to Squirt.

3.4. TID Velocity

While the spectral analysis provides information on how the peak amplitude of the TID changes as it propagates from north to south, it also supplies information on the phase of the wave, which can be used to calculate the TID velocity. To calculate the velocity of the 26 January 2014 TID, two techniques are applied to the data; the first evaluates ionograms for hook signatures, and the second uses the spectral analysis phase difference between two ionosondes.

The first technique calculates TID velocity by analyzing ionograms. Given that a hook signature on an ionogram indicates the presence of a TID (Figure 2), ionograms are evaluated at each ionosonde over time. The time a hook first appears on an ionogram is recorded for each site, and a time difference is calculated to determine how long it takes the TID to propagate from one ionosonde to another. From this time difference and a known distance between ionosondes, the velocity, v, $(\mathrm{m\,s^{-1}})$ is $v = d/\Delta t$, where d is the distance between ionosondes (m), and Δt is the time difference between hook initiation (s).

During the TID period, the first hook signature is observed on the Kirtland ionogram at 1911 UT. Table 3 outlines the time progression of the southward propagating TID, as determined by the time a hook is first observed on the ionogram at each ionosonde. From these times, the TID velocity for each of the ionosonde pairs can be calculated (Table 4). The Kirtland and Squirt ionosondes are separated by 288 km.

Table 3. Time the hook signature is first observed on the ionogram at each ionosonde.

Ionosonde	Time (UT)
Kirtland	1911
Munyo	1927
Cherry	1934
Squirt	1937

43

The time difference in these ionogram measurements is 26 minutes, which means the TID velocity between Kirtland and Squirt is $185\,\mathrm{m\,s^{-1}}$. Decreasing the distance between ionosondes, decreases the time difference. Kirtland and Munyo ionosondes are $160\,\mathrm{km}$ apart; the time difference in hook signatures is 16 minutes, which yields a TID velocity of $167\,\mathrm{m\,s^{-1}}$. However, if the distance between ionosondes becomes too short, the TID velocity becomes questionable. The Cherry and Squirt ionosondes are separated by $55\,\mathrm{km}$. The time difference in ionogram measurements is 3 minutes, indicating the TID velocity is $305\,\mathrm{m\,s^{-1}}$, nearly 1.4 to 1.8 times greater than the TID velocity for the other five ionosonde pairs.

To calculate the error in ionogram based velocity measurements, the cadence of ionosonde measurements is considered. The ionosondes at Kirtland, Munyo, and Squirt took measurements every 6 minutes, while the Cherry ionosonde was every 2 minutes. Consequently, despite the first appearance of the hook on the Kirtland ionogram at 1911 UT, the hook may have appeared as early as 5 minutes prior (1906 UT), during which no ionogram measurements were available; the ionogram displays 1 minute measurements and the ionosonde cadence is 6 minutes ($6 - 1 = 5$). The error in each of the ionograms is based on the cadence of ionosonde measurements as reported in Table 5. One interesting note is that the potential error at Squirt, 5 min-

Table 4. TID velocity measurements from the time a hook signature is first observed on the ionogram at each ionosonde.

Ionosonde Pair	Distance (km)	Δt (min)	Velocity ($\mathrm{m\,s^{-1}}$)
Kirtland-Squirt	288	26	185
Kirtland-Cherry	234	23	169
Kirtland-Munyo	160	16	167
Munyo-Squirt	131	10	219
Munyo-Cherry	77	7	183
Cherry-Squirt	55	3	305

44

Table 5. Table of the potential error in the time the hook is observed on the ionogram. This error results from the cadence at which ionosonde measurements occur; therefore, the 6 minute cadence at Kirtland implies that the hook may be observed as early as 1906 UT if the error was in the northern ionosonde.

Ionosonde	Time (UT)	Maximum Error (min)	Error in Northern Site (UT)	Error in Southern Site (UT)
Kirtland	1911	-5	1906	
Munyo	1927	-5	1922	1922
Cherry	1934	-1		1933
Squirt	1937	-5		1932

utes, is greater than the 3 minute time difference it took the TID to travel between Cherry and Squirt (Table 4); therefore, this circuit is removed from all ionogram TID velocity calculations. With the Cherry to Squirt circuit removed from Table 4, the TID velocities as measured from ionograms are: maximum is $219 \, \mathrm{m \, s^{-1}}$, minimum is $167 \, \mathrm{m \, s^{-1}}$, and average is $184 \, \mathrm{m \, s^{-1}}$.

The error bounds in TID velocity measurements for the ionogram is found by defining the negative error, as the velocities when the northern site is misrepresented, and the positive error, when the southern site is misrepresented. That is, if the northern site is the ionogram with the error, the hook does not occur at 1911 UT at Kirtland, but instead at 1906 UT. Therefore, the time difference as the TID travels from Kirtland (1906 UT) to Squirt (1937 UT) is 31 minutes as opposed to 26 minutes with no error. Likewise, if the southern site is the ionosonde with the error, the hook occurs earlier at the southern site. Consequently, the time difference between Kirtland (1911 UT) to Squirt (1932 UT) is 21 minutes with the error at the souther site. Table 6 provides the negative and positive error bounds in the TID velocity as measured from the ionograms, indicating that the negative error in TID velocities differ by $48 \, \mathrm{m \, s^{-1}}$, while the positive error in TID velocities vary by $261 \, \mathrm{m \, s^{-1}}$. The large variance in the positive error is a result of the short separation distance between

45

Table 6. Ionogram velocity measurement error bounds. The negative error results when the hook occurs during the error period at the northern site and the positive error is when the hook occurs during the error period in the southern site.

Ionosonde	Negative Error		Positive Error	
	Δt (min)	Velocity (m s^{-1})	Δt (min)	Velocity (m s^{-1})
Kirtland-Squirt	31	155	21	288
Kirtland-Cherry	28	139	22	177
Kirtland-Munyo	21	127	11	243
Munyo-Squirt	15	146	5	438
Munyo-Cherry	12	107	6	213

ionosondes; thus, a small decrease in the time difference results in a large velocity increase. This is illustrated in Table 6 for the Munyo to Squirt circuit, 131 km apart. When the southern site, Squirt, is the source of the error, the time difference decreases from 10 to 5 minutes, and the velocity doubles to 438 m s^{-1}, which is much greater than the surrounding measurements.

The second technique calculates TID velocity by analyzing the spectral phase difference in the dominate waves between ionosondes. Figure 36 shows the phase as a function of period for each ionosonde calculated using DFT. To calculate a TID velocity, the phase of the wave is extracted for both 45 and 60 minutes periods to determine the propagation time between ionosondes. To eliminate the 2π phase ambiguity, the time and velocity measurements are plotted over integer values of k, ranging from -2 to +2. The time difference, Δt (min), is

$$\Delta t = \left(\Delta\Phi + k(2\pi)\right)\left(\frac{period}{2\pi}\right) \tag{8}$$

where $\Delta\Phi$ is the phase difference in radians (southern ionosonde subtracted from the northern ionosonde to capture the direction of the wave) at a given period. The time differences for the 45 and 60 minute period, for each k-value, are averaged for the

46

ionosonde pair distances as shown in Figure 37. To determine which k-value represents the actual time difference, the time difference from previous ionogram measurements are referenced. The ionogram measurements suggest the maximum time difference is near 30 minutes and decreases as the distance between ionosondes decrease. Figure 37 shows a descending distance along the x-axis, and the correct k-value average time difference is highlighted by the red box; k = 1 for the first three circuits, and k = 0 for the last two circuits, giving an average time difference of 40 minutes decreasing to 10 minutes.

From the average time difference calculated in Equation 8 for each ionosonde pair, the velocity for the 45 and 60 minute periods are averaged for each k-value, as shown in Figure 38. The selected k-values that applied to the average time difference in Figure 37, also pertain to the selected k-values (highlighted by the red box) in
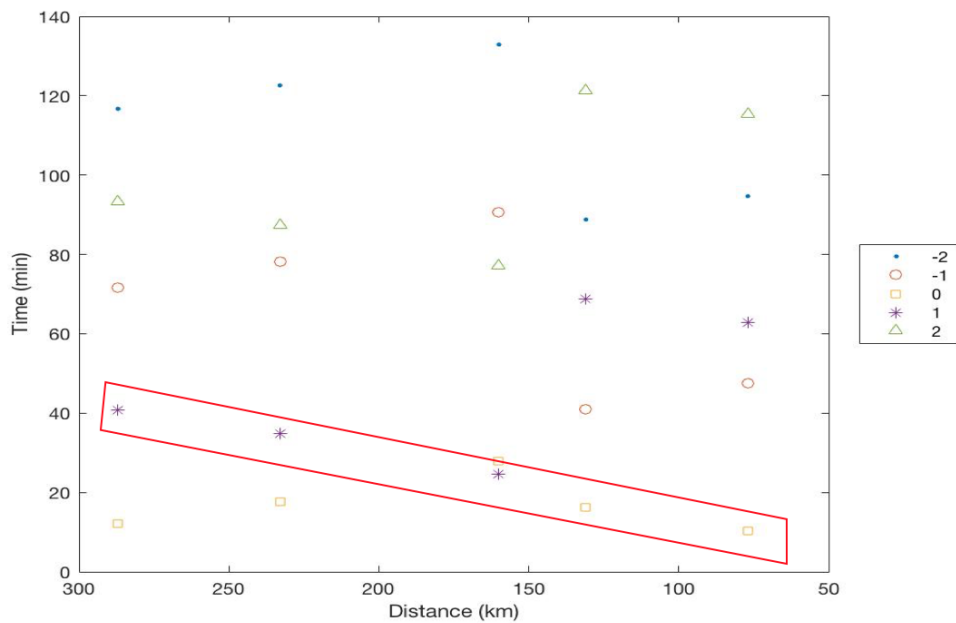
Figure 37. Average time difference, Δt, for each k-value given the spectral phase difference at each ionosonde. Previous ionogram measurements suggest the Δt should be near 30 minutes and decrease as the the distance between ionosondes decrease; therefore, the red box indicates the selected Δt for a given distance.

47

Figure 38. The average TID velocity between each ionosonde pair calculated from the spectral phase difference is reported in Table 7.

The results of the two techniques used to measure TID velocity on 26 January 2014 are shown in Figure 39. Ionogram measurements indicate the TID average velocity is $184\,\mathrm{m\,s^{-1}}$, while the spectral phase difference suggests $122\,\mathrm{m\,s^{-1}}$. Unfortunately, this velocity difference is too great to say which technique is accurate; therefore, a third technique is applied to validate the correct method.

The third technique utilizes a temporal cross-correlation of AoA elevation angles. Given the southward propagation of the TID on 26 January, a cross-correlation is performed between G10-GRN and the following AoA sites: G10-PND, G10-FRN, and G10-RDS1. Figure 40 shows the AoA elevation angles for G10-GRN and each of these AoA sites. A positive time shift is applied to G10-GRN AoA elevation angles, to find the time shift that maximizes the correlation in the two AoA measurements. Figure
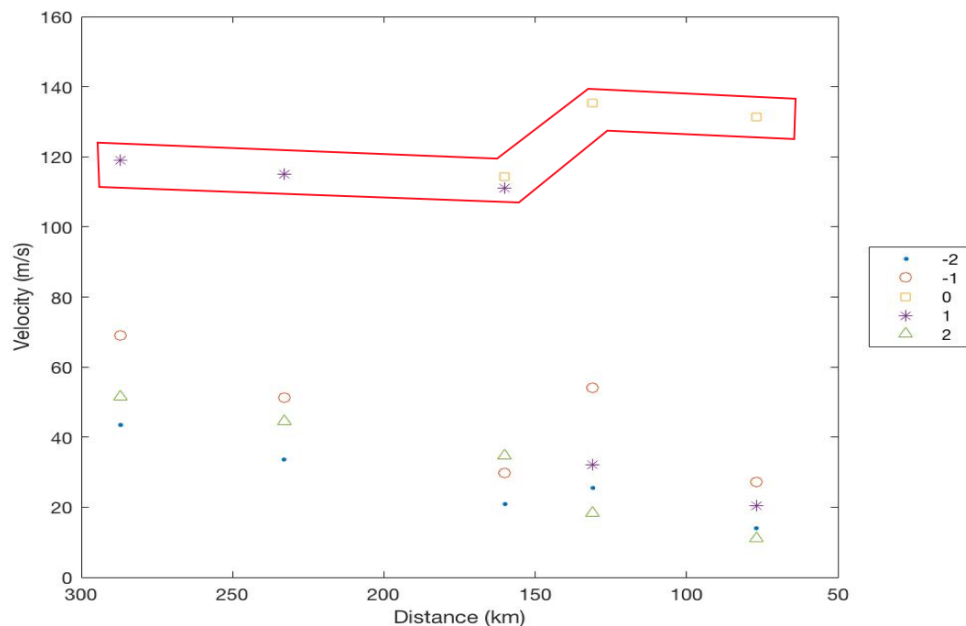
Figure 38. Average TID velocity based on spectral phase difference for k-values. Velocity is computed using the respective k-value selected Δt from Figure 37.

48

Table 7. TID velocity as measured by spectral phase difference in the dominate waves between ionosondes.

Ionosonde Pair	Distance (km)	Velocity $\mathrm{m\,s^{-1}}$
Kirtland-Squirt	288	119
Kirtland-Cherry	234	115
Kirtland-Munyo	160	111
Munyo-Squirt	131	135
Munyo-Cherry	77	131
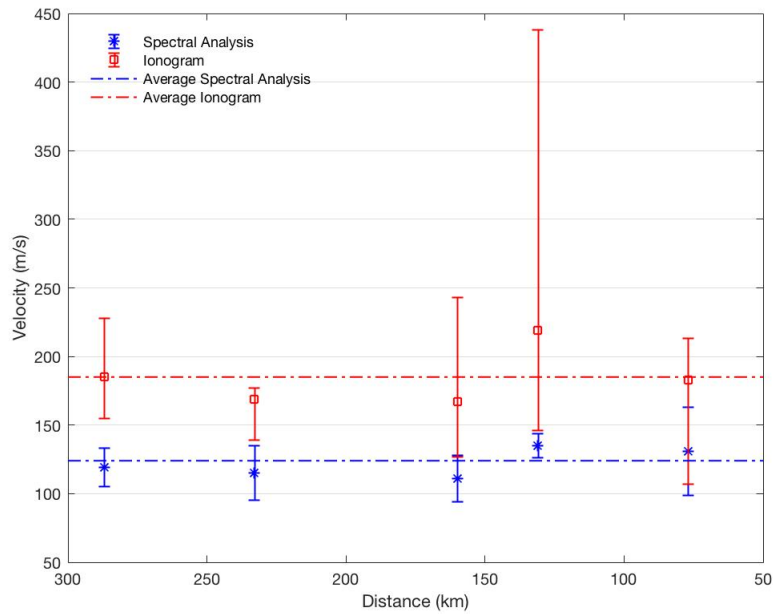
Figure 39. TID average velocity measurements on 26 Jan 2014 from 1900-2200 UT. Average velocity based on ionogram measurements is 184 m s^{-1} and from spectral phase differences is 122 m s^{-1}.
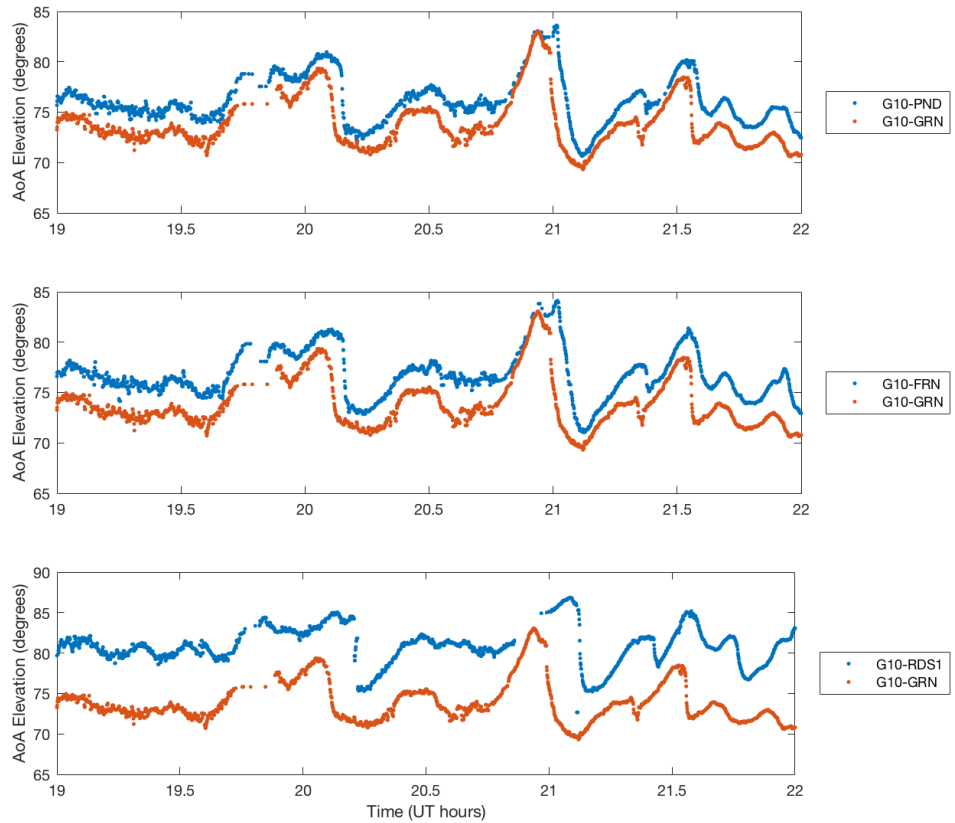
Figure 40. AoA elevation angles for 5.34 MHz frequency on 26 Jan 2014 from 1900-2200 UT. A temporal cross-correlation is performed on G10-GRN for each plot to reveal the velocity of the TID from AoA measurements.

41 reveals that an ∼2 minute time shift to G10-GRN measurements maximizes the correlation with the two northern sites (G10-PND and G10-FRN), while a 5 minute 30 second time shift is needed at the southern site (G10-RDS1). Therefore, we assume a MM to use the midpoint and the time shift maximizing the correlation, the average TID velocity is calculated to be $111 \, \mathrm{m \, s^{-1}}$. Comparing the average TID velocity from the AoA temporal cross-correlation with that of the ionogram and spectral analysis phase difference indicates the accurate TID velocity to be from the spectral analysis at $122 \, \mathrm{m \, s^{-1}}$.

50
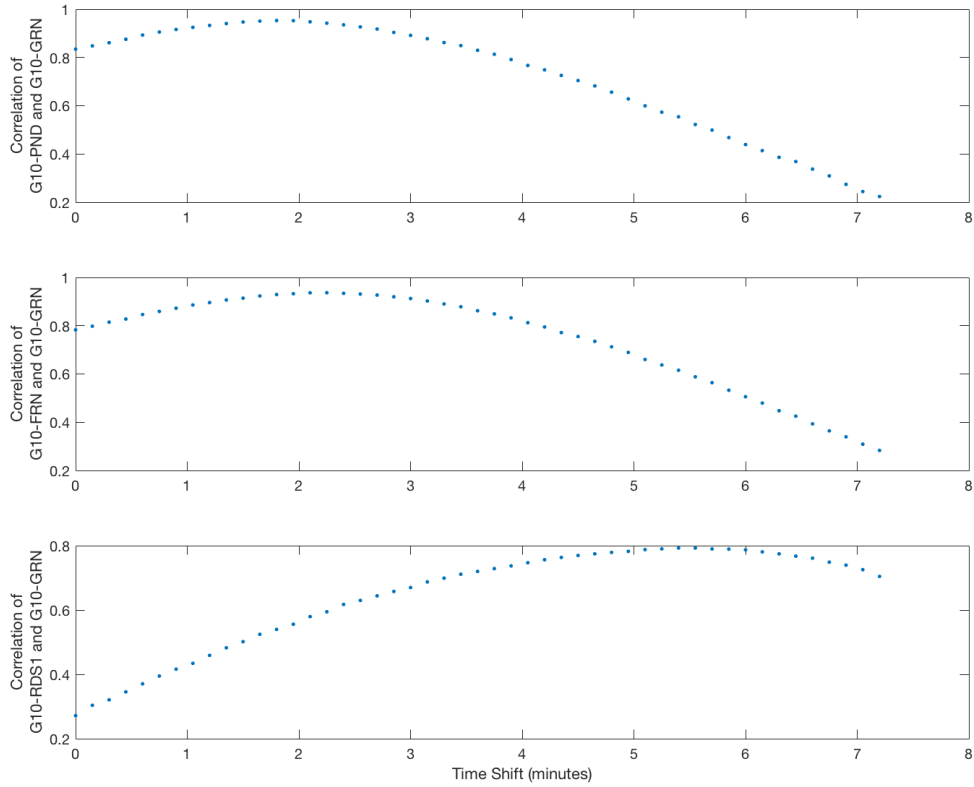
Figure 41. Cross-correlation of AoA elevation angles from Figure 40 reveals the time shift in G10-GRN AoA elevation angle required to gain the highest correlation amongst the two AoA sites. Top: Peak correlation between G10-PND and G10-GRN is achieved at a 1 minute 48 second time shift. Middle: Peak correlation between G10-FRN and G10-GRN is achieved at 2 minute 15 second time shift. Bottom: Peak correlation between G10-RDS1 and G10-GRN is achieved at a 5 minute 30 second time shift.

From the TID velocity and period, the wavelength can be calculated using the dispersion relation

$$\omega = vk \tag{9}$$

$$\implies \lambda = v\tau \tag{10}$$

where ω is the TID frequency, v is the velocity, k is the wavenumber, λ is the wave-

51

length, and τ is the period. Velocities calculated from the spectral phase differences for the 45 and 60 minute periods are displayed along with calculated wavelengths from the dispersion relation in Figure 42. An average wavelength of 394 km is calculated for the TID, with a range of 255 to 587 km. Given a TID with this wavelength, a velocity of $122\,\mathrm{m\,s^{-1}}$ and a period of 36 to 60 minutes, the TID observed on 26 January 2014 is characterized as a MSTID.
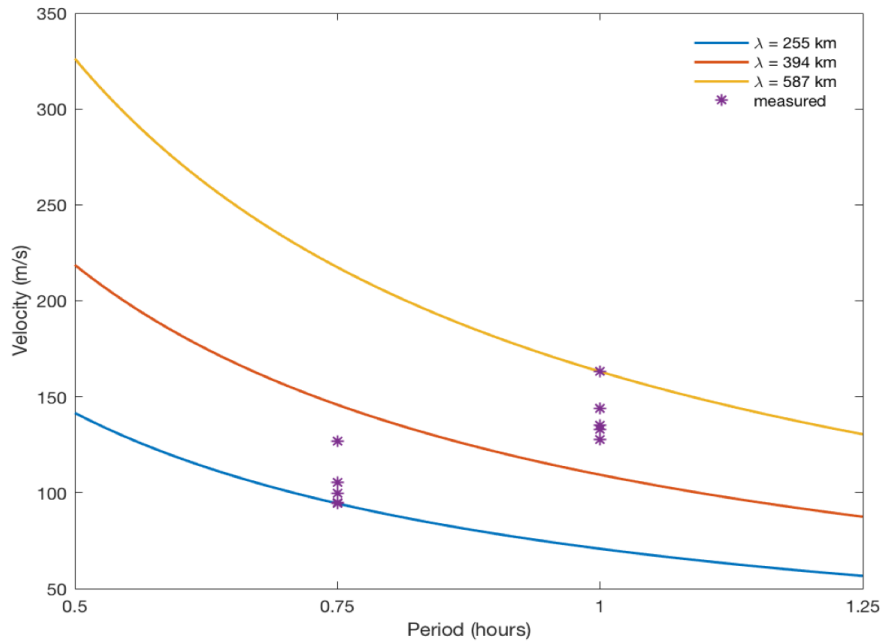
Figure 42. TID wavelengths calculated from the dispersion relation, $\omega = vk$, using the velocities calculated from the spectral phase differences for the 45 and 60 minute periods. The solid lines show the dispersion relation for the minimum, average, and maximum wavelengths. The points represent the measured velocities derived from spectral phase differences.

3.5. Temporal Cross-Correlation

The accurate TID velocity is revealed using a temporal cross-correlation of AoA elevation angles; a similar approach is used to compare time-shifted ionosonde virtual heights with AoA elevation angles to determine if a shift in time can reproduce the large correlations observed for co-located measurements. A temporal cross-correlation is performed for each of the four ionosondes against the G10-POL AoA elevation angles. Figure 43 shows the G10-POL AoA elevation angle and Kirtland ionosonde virtual height measurements, where the two sites are separated by 230 km. In the right figure, the ionosonde virtual heights are time shifted +60 minutes. This time shift takes place over 100 steps to determine how the AoA elevation angle and ionosonde virtual height measurements are correlated at each step in time. Figure 44 indicates that the G10-POL AoA elevation angle and Kirtland ionosondes virtual height measurements have the highest correlation, 0.36, at a time shift of 42 minutes. This suggests that 42 minutes after the TID passes Kirtland, it will impact the G10-POL
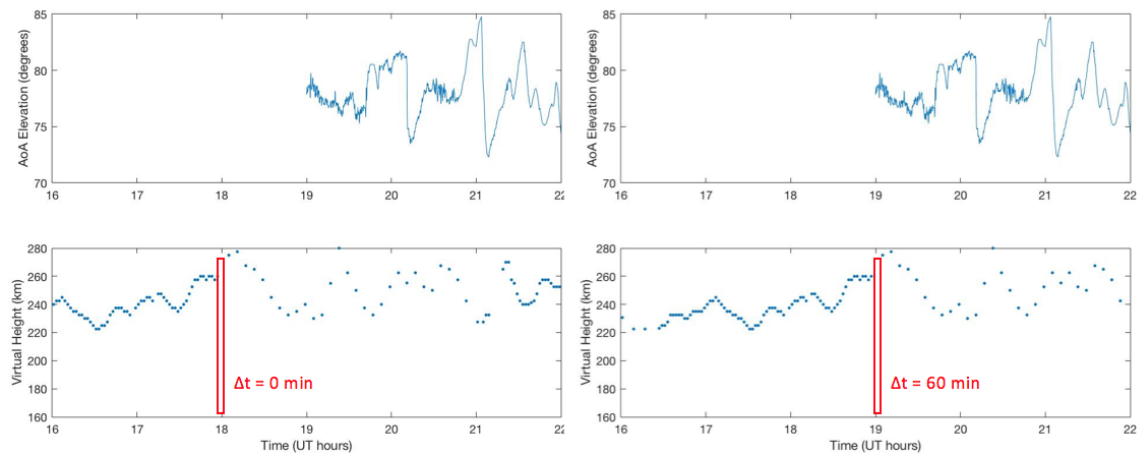
Figure 43. Two figures of G10-POL AoA elevation angle and Kirtland ionosonde virtual height measurements during TID period. The figure on the left is the ionosonde virtual height measurements observed at Kirtland with no time shift, and the figure on the right are the same measurements after a +60 minute time shift is applied to the virtual heights.

53
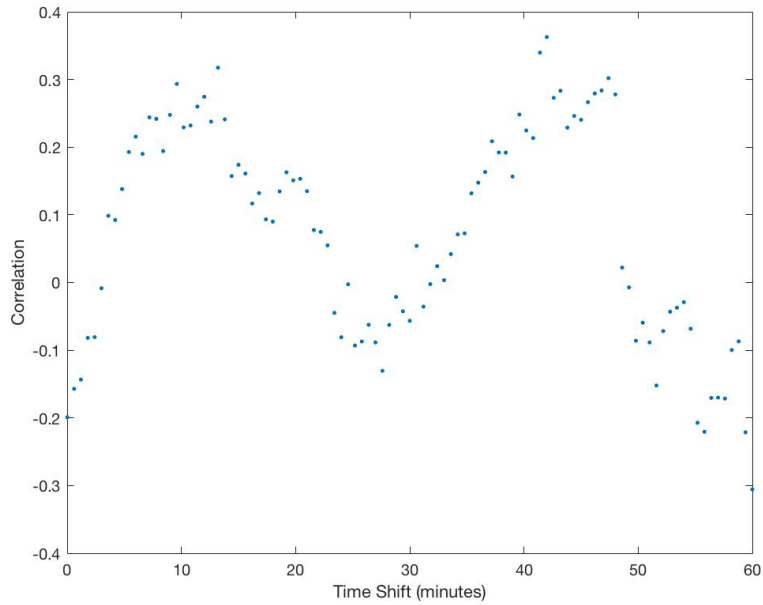
Figure 44. Temporal cross-correlation of G10-POL AoA elevation angle and Kirtland ionosonde virtual height for 26 Jan 2014 from 1900-2200 UT. These sites are 230 km apart. The peak correlation is 0.36, and occurs at a 42 minute time shift.

circuit. However, the velocity of the TID is $122\,\mathrm{m\,s^{-1}}$, which means the expected time shift for peak correlation between Kirtland ionosonde virtual heights and G10-POL AoA elevation angles should be 31 minutes. The difference in the expected and cross-correlation time shifts, as well as the weak correlation value, indicate the TID wave characteristics change as the TID propagates from Kirtland to G10-POL midpoint.

This same temporal cross-correlation is repeated for each of the remaining three ionosondes against the G10-POL AoA elevation angles. A +60 minute time shift is performed for both Munyo and Cherry; however, a -60 minute time shift is performed for Squirt. The negative time shift accounts for the location of Squirt ionosonde with respect to G10-POL, as the TID propagates from north to south. Figure 45 shows the cross-correlation for measurements from G10-POL midpoint and Munyo, which are 73 km apart. This cross-correlation reveals a moderately positive correlation, 0.55, after a 9 minute time shift. Given the TID velocity, the expected time shift is

54
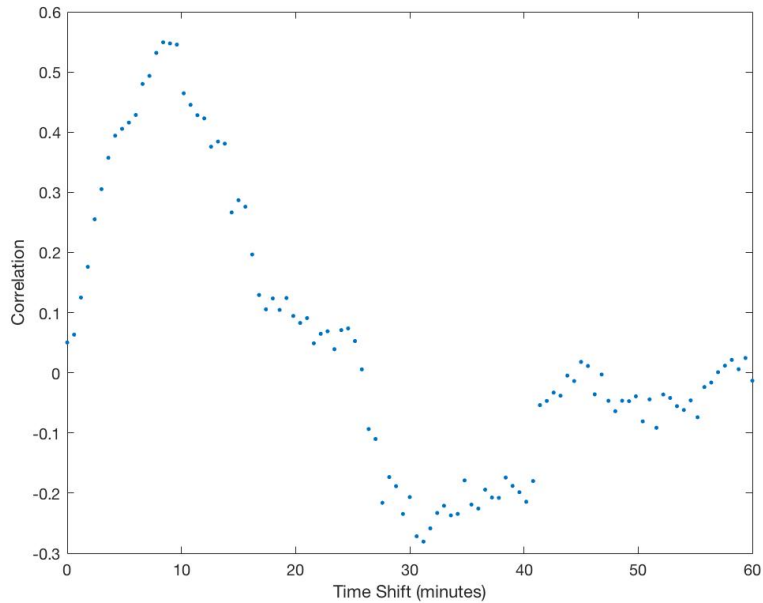
Figure 45. Cross-correlation of G10-POL AoA elevation angle and Munyo ionosonde virtual heights vs time shift on 26 Jan 2014. These two sites are separated by 73 km. The peak correlation value is 0.55, and occurs at a time shift of 9 minutes.

10 minutes. The small difference in expected and cross-correlation time shifts, along with a moderately positive correlation value, suggests the TID characteristics are more similar between Munyo and G10-POL than for Kirtland and G10-POL midpoint.

The next cross-correlation between G10-POL midpoint and Squirt, 58 km apart, is shown in Figure 46, which reveals that the maximum correlation of 0.24 occurs after a time shift of 8 minutes and matches what is expected based on TID velocity. The last cross-correlation is shown in Figure 47 between G10-POL and Cherry, 5.7 km apart. As expected due to the close proximity, these two sites are strongly correlated at 0.73, after a time shift of less than 1 minute. The cross-correlation time shift matches the expected time shift based on the TID velocity. Therefore, given the same time shifts and strong correlation value, the TID will possess very similar characteristics at Cherry and the G10-POL midpoint.

Figure 48 shows the temporal cross-correlation of G10-POL AoA elevation angle

55
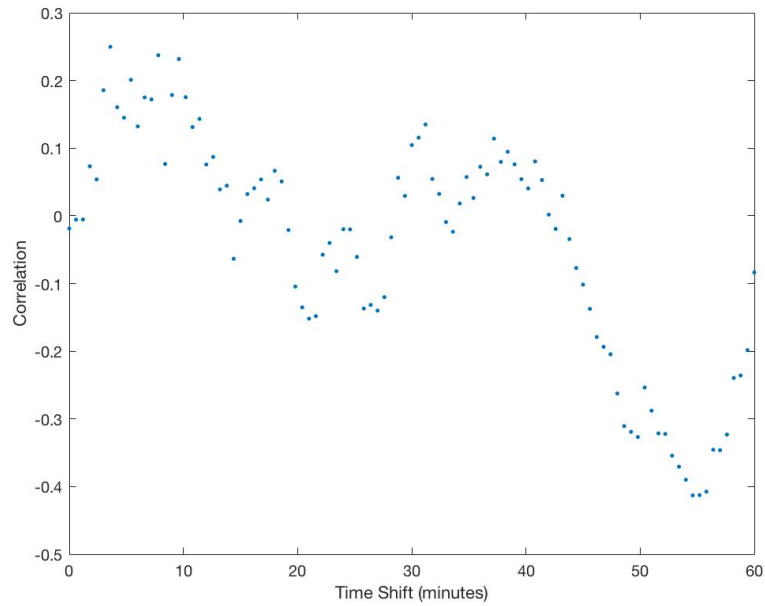
Figure 46. Cross-correlation of G10-POL AoA elevation angle and Squirt ionosonde virtual height vs time shift on 26 Jan 2014. The two sites are separated by 58 km. The peak correlation value is 0.24, and occurs at a time shift of 8 minutes.
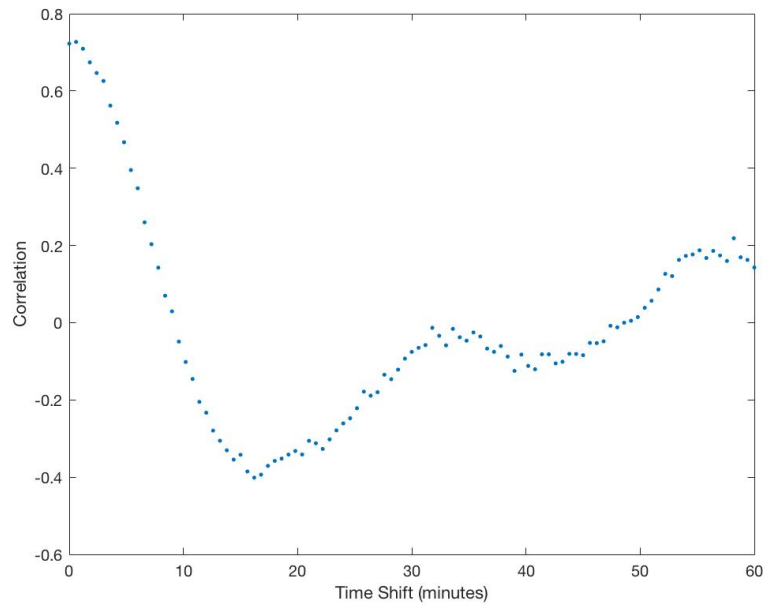
Figure 47. Cross-correlation of G10-POL AoA elevation angle and Cherry ionosonde virtual height vs time shift on 26 Jan 2014. The two sites are separated by 5.7 km. The peak correlation value is 0.73, and occurs at a time shift of less than 1 minute.

56

with each of the four ionosondes. This shows the peak correlation, 0.73, is achieved at Cherry 5.7 km from the G10-POL midpoint. As the separation distance between the G10-POL midpoint and ionosonde increases to 58 km at Squirt, the peak correlation decreases to 0.24, at Munyo 73 km away it is 0.55, and at Kirtland 230 km away it is 0.36. Although time shifting ionosonde virtual heights improves the correlation, when the separation distance is too great, the correlation remains weak due to changes in TID wave structure over time. Additionally, if the expected time shift given the TID velocity matched the cross-correlation time shift, it would indicate that the wave structure did not change as it wave propagates south and that the temporal cross-correlation could be used with confidence to estimate the time a TID would impact an AoA midpoint. The expected and cross-correlation time shifts at Cherry, Munyo, and Squirt are the nearly the same; however, the time difference at Kirtland is 11 minutes longer than the expected time difference. This suggests the cross-correlation method works well within 75 km; however, at greater distances the cross-correlation should not be used to estimate the time a TID impacts an AoA midpoint.
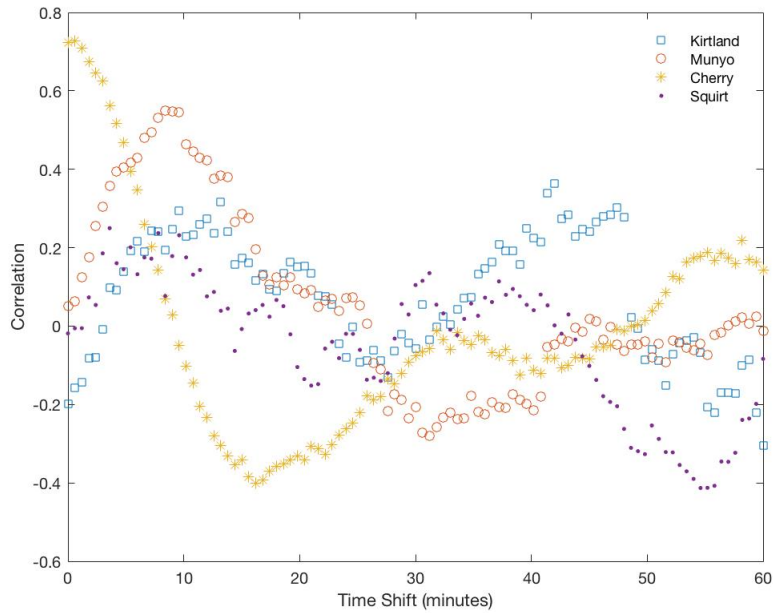
Figure 48. Temporal cross-correlation of G10-POL AoA elevation angles and each of the four ionosonde's virtual height measurements. The peak correlation varies as a function of distance; the peak correlation for Cherry at ∼6 km is 0.73, Squirt at 58 km is 0.25, Squirt at 73 km is 0.55, and Kirtland at 230 km is 0.36.

58

3.6. Predicted AoA Elevation Change

The final assessment of this research is to determine whether virtual height measurements from two upstream ionosondes, can predict a change in AoA elevation angles at a downstream midpoint link during a TID. To test this approach, a simple model is applied to data from the upstream ionosondes during a TID event. The simple model assumes: the MM is valid, tilts are ignored, and the distance between transmitter and receiver are known. The TID velocity is calculated using spectral phase difference from two upstream ionosondes, then uses the closest ionosonde for virtual height measurements.

The first analysis evaluates the simple model using Kirtland and Munyo ionosonde spectral phase difference to calculate TID velocity and Munyo ionosonde virtual height measurements to predict AoA elevation angle changes at the G10-POL midpoint link. Figure 49 shows the AoA elevation angles and virtual height measurements for G10-POL and Munyo using the 5.34 MHz frequency on 26 January 2014 during the TID period. The horizontal MM with no tilts is applied to Munyo ionosonde virtual height measurements, to calculate the MM AoA elevation angle. Similar to Equation 7, the calculation for the MM AoA elevation angle (rad), ϵ_{mm}, is

$$\epsilon_{mm} = \arctan\left(\frac{2h}{d}\right) \qquad (11)$$

where h is the virtual height measured at Munyo (km), and d is the distance between the transmitter and receiver (km), 73 km for G10-POL. Figure 50 shows the resulting MM AoA elevation angles for G10-POL calculated using Munyo ionosonde virtual heights. A comparison of how the G10-POL MM and actual AoA elevation angles relate is displayed in Figure 51. No time shift has been applied to the ionosonde derived MM elevation angles; when the TID is measured at Munyo, it has not reached

59
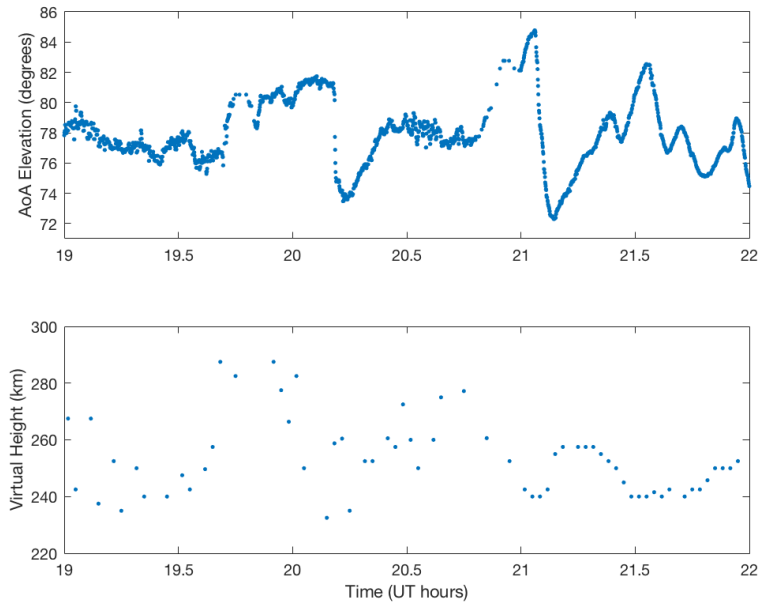
Figure 49. G10-POL AoA elevation angle and Munyo ionosonde virtual heights for 5.34 MHz frequency on 26 Jan 2014 from 1900-2200 UT, during the TID period. Notice Munyo virtual heights increase prior to 1930 UT; however, AoA elevation angles do not increase until 1940 UT. This is due to the geographical separation between the ionosonde and AoA circuit.

the G10-POL midpoint link. This delay causes the MM AoA elevation angle to start increasing shortly before 1930 UT, while the actual AoA elevation angle does not increase until closer to 1940 UT. To account for this time delay, a time shift needs to be applied to the MM AoA elevation angles in Figure 51.

To find the amount of time the MM AoA elevation angle must be shifted, the TID velocity and distance from the ionosonde to AoA midpoint link must be known. The TID velocity is measured at $111\,\mathrm{m\,s^{-1}}$ from the spectral phase difference between the Kirtland and Munyo ionosondes. Additionally, the distance between the Munyo ionosonde and G10-POL link midpoint is 73 km. From the TID velocity and distance from the Munyo ionosonde, the time shift required is 11 minutes. This time shift is applied to the MM AoA elevation angles in Figure 51 to account for the geographical separation between ionosonde and AoA circuit midpoint. The time shifted MM AoA

60
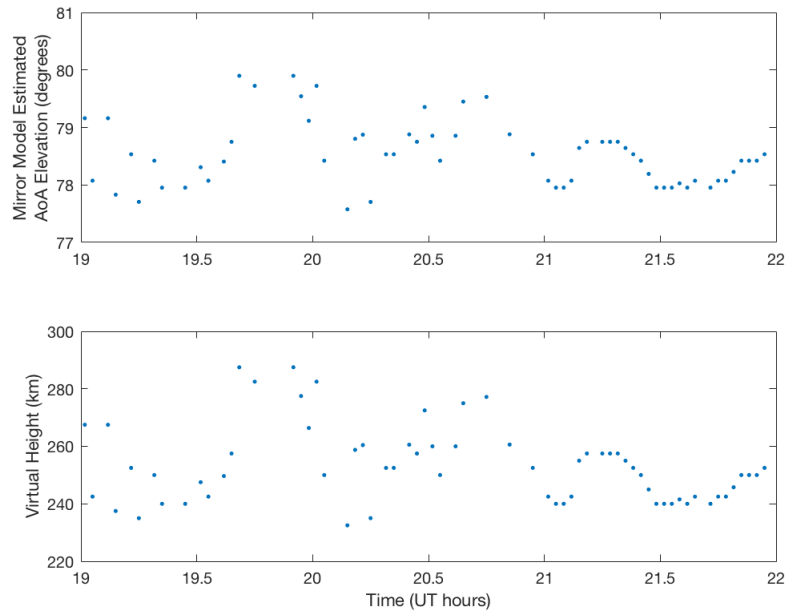
Figure 50. Estimation of G10-POL AoA elevation angles given application of the MM using Munyo ionosonde virtual heights during the TID period. Top: G10-POL MM estimated AoA elevation angles. Bottom: Munyo ionosonde virtual heights.

elevation angles are shown in Figure 52 along with the actual AoA elevation angles. The time shifted MM does relatively well at predicting the trend early on; however, the magnitude by which the MM AoA elevation angle changes, does not match the actual AoA elevation angle.

The difference in the time shifted MM and actual AoA elevation angles for G10-POL are shown in Figure 53. The average difference between the predicted and measured angles is -0.6°. A maximum difference of 5.3° is observed near 21 UT. This suggests that the change in AoA elevation angle is not due to only a change in height as the simple MM implies, but also strongly depends on changes in the tilt of the ionosphere at the reflection point.

Further evidence that the tilt is responsible for the change in AoA elevation angles, and not the height as the simple MM implies, is shown in Figure 54. The North-South tilt measurements in this figure are measured by the Munyo ionosonde. Similar to

61
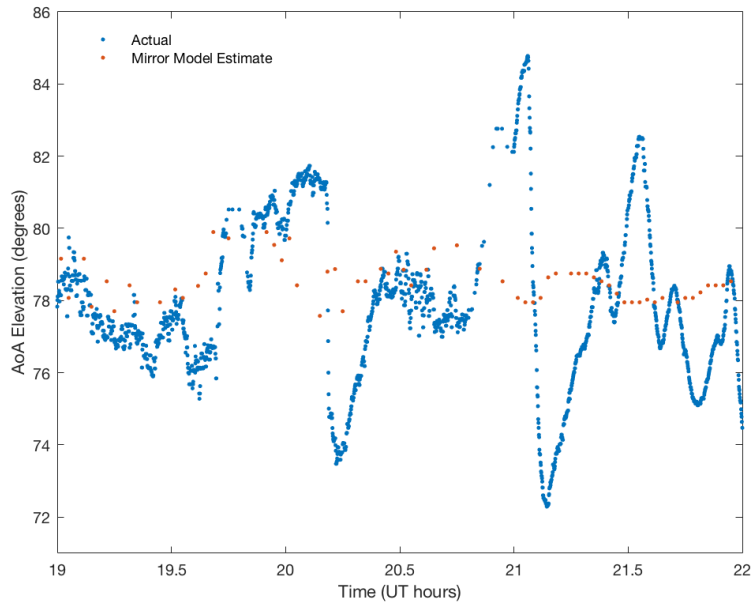
Figure 51. Plot of actual G10-POL AoA elevation angles from Figure 49 with the simple MM AoA elevation angles plotted in Figure 50. Similar to Figure 49, this reveals that the TID passes Munyo prior to the G10-POL midpoint link; therefore, the MM AoA elevation angles need to be time shifted to ensure the simple MM is compared to the actual AoA measurements as the TID passes G10-POL.

the MM AoA elevation angles, Munyo tilt measurements are time shifted 11 minutes to account for the time delay. The simple MM performs well when the tilt is near 0°, which is exhibited at 1921 UT when the tilt is almost 0° and the difference in MM and actual AoA elevation angles is -0.3°. However, as the tilt measurements increase, so does the difference between the predicted and measured elevation angles, as shown near 2100 UT when the tilt is -4.4° and the angle difference is 5.3°. Note that this analysis is only for the AoA elevation angle and the ionosonde North-South tilt. To get a more accurate representation, the AoA azimuth angle and ionosonde East-West tilt measurements should also be incorporated; however, until that information can be applied, this simple MM can be used for geolocation when the ionosonde tilt measurements are near 0°.

To calculate the maximum change in AoA elevation angles for the simple MM
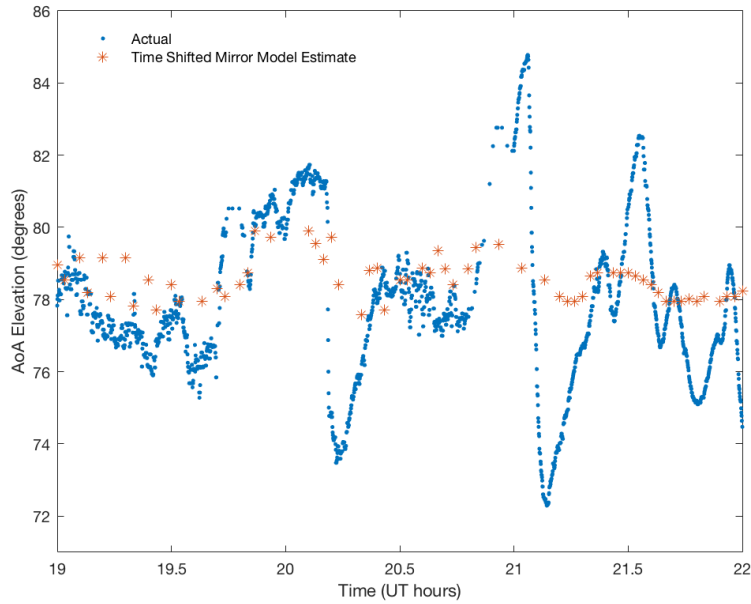
Figure 52. MM AoA elevation angles from Figure 51 are time shifted based on the TID velocity and distance between Munyo and G10-POL. This allows a comparison of both data sets when the TID is over G10-POL.
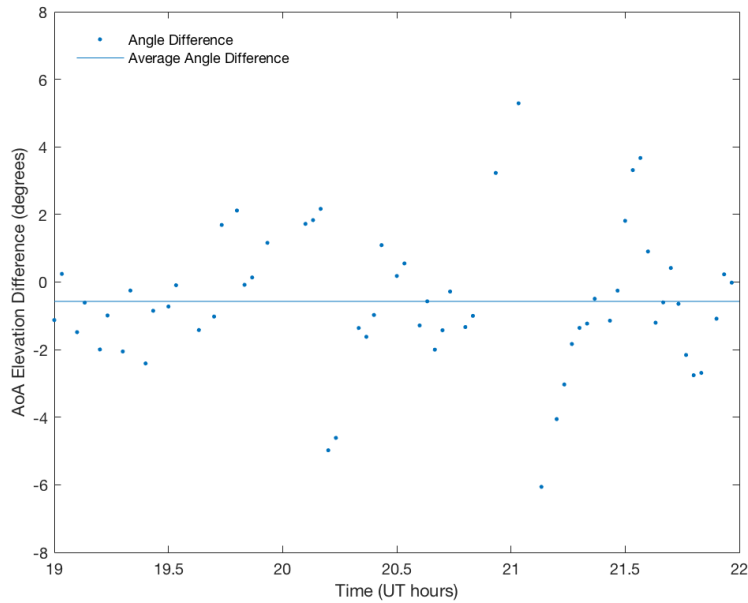
Figure 53. Difference in G10-POL actual and time shifted MM AoA elevation angles using virtual heights from Munyo. The average angle difference is -0.6°, highlighted by the solid line.

63
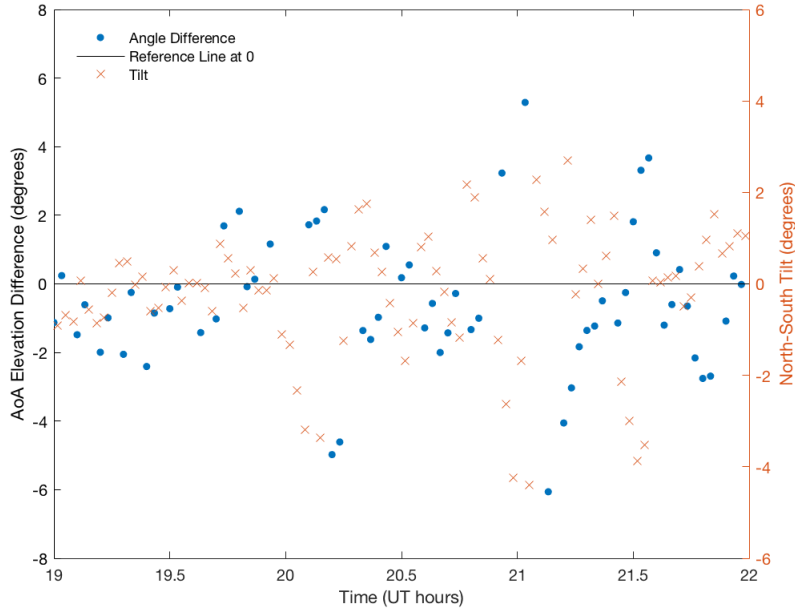
Figure 54. Plot to compare the simple MM for G10-POL with the time shifted Munyo ionosonde North-South tilt measurements. When the tilt is near 0° (horizontal reference line), the angle difference in the MM and actual AoA elevation angles is small which suggests the simple MM performs well. However, as the tilt increases, so too does the angle differences and the simple MM should not be considered.

based on the maximum change in virtual heights, a derivative of Equation 11 with respect to height is required:

$$
\begin{aligned}
\frac{d\epsilon}{dh} &= \frac{2d}{d^2 + 4h^2} \\
&= \frac{2d}{d^2(1 + \frac{4h^2}{d^2})} \\
&= \frac{2}{d(1 + \frac{4h^2}{d^2})}
\end{aligned}
\tag{12}
$$

where $d\epsilon$ is the change in AoA elevation angle (radians), dh is the change in ionosonde virtual height (km), d is the distance between transmitter and receiver (km), and h

is the ionosonde virtual height (km). Additionally, applying the relation

$$\frac{4h^2}{d^2} = \tan^2(\epsilon) \tag{13}$$

to Equation 12, the change in AoA elevation angle is

$$\begin{aligned}
\frac{d\epsilon}{dh} &= \frac{\tan(\epsilon)}{h(1 + \tan^2(\epsilon))} \\
\implies \Delta\epsilon &= \frac{\tan(\epsilon_0)}{h_0(1 + \tan^2(\epsilon_0))}\Delta h
\end{aligned} \tag{14}$$

where ϵ_0 is the initial AoA elevation angle corresponding to h_0, h_0 is the average ionosonde virtual height prior to the TID, and Δh is the greatest change in ionosonde virtual heights from h_0 measured during the TID. From previous ionogram analyses, it is known that the TID passes Munyo between 1922 and 1927 UT; therefore, from Figure 49, an average of the Munyo ionosonde virtual heights prior to the TID passage reveals h_0 is 243 km. The greatest virtual height measured during the TID is 288 km, thus Δh is 45 km. Lastly, the AoA elevation angle, ϵ_0, is 77.2°. Applying these values to Equation 14 the maximum change in AoA elevation angle, given measurements at Munyo and G10-POL, is 2.3°.

The maximum change in AoA elevation angle, calculated by Equation 14 is compared to the actual and time shifted MM AoA elevation angles during the TID to analyze the accuracy of this approach. The time shifted MM AoA elevation angle changes by a maximum of 1.9°, and the actual AoA elevation angle changes by a maximum of 6.4° during the TID. Therefore, Equation 14 overestimates the maximum change in time shifted MM AoA elevation angle by 0.4°, and underestimates the maximum change in actual AoA elevation angle by 4.2°. This indicates that the tilt of the ionosphere at the reflection point is crucial in estimating AoA elevation angle during a TID.

65

The simple model analysis is repeated to predict the change in AoA elevation angle at G10-GRN during the same TID period. Figure 55 shows the actual G10-GRN AoA elevation angle and Munyo virtual height measurements during this time. Analysis of the virtual heights and elevation angles reveals the TID passes Munyo near 1925 UT and G10-GRN midpoint at 1936 UT. The simple MM AoA elevation angles for G10-GRN, along with the Munyo virtual height measurements are shown in Figure 56, using a distance of 52 km between Munyo and G10-GRN midpoint. Figure 57 reveals the MM AoA elevation angles at a zero time shift, which shows the MM AoA elevation angles increase near 1925 UT, and the actual AoA elevation angles increase around 1936 UT. To account for the time delay, a time shift is applied to the MM AoA elevation angles.

The same principles for finding the time shift in the first analysis at G10-POL, are applied to G10-GRN MM AoA elevation angles. Given the TID velocity, as
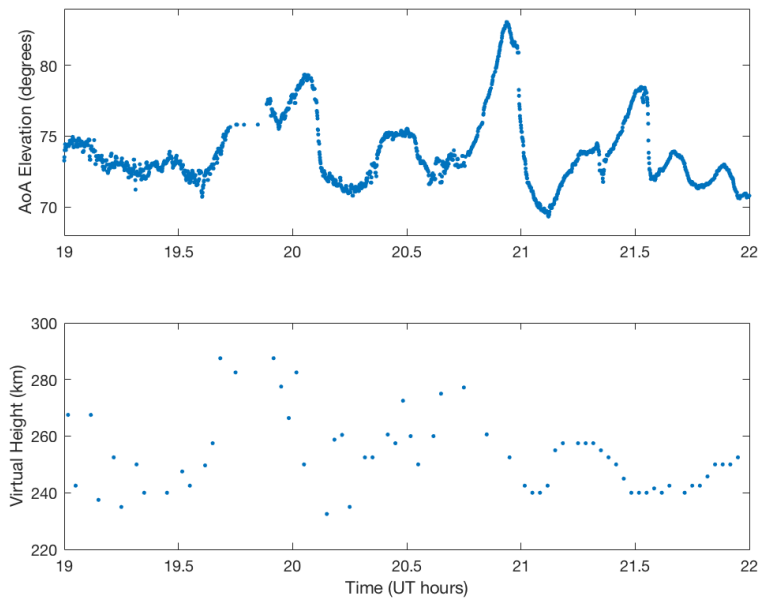
Figure 55. G10-GRN AoA elevation angle and Munyo ionosonde virtual heights during the TID period. This reveals the TID passes Munyo near 1925 UT and G10-GRN at 1936 UT as the virtual heights and elevation angles increase.

66
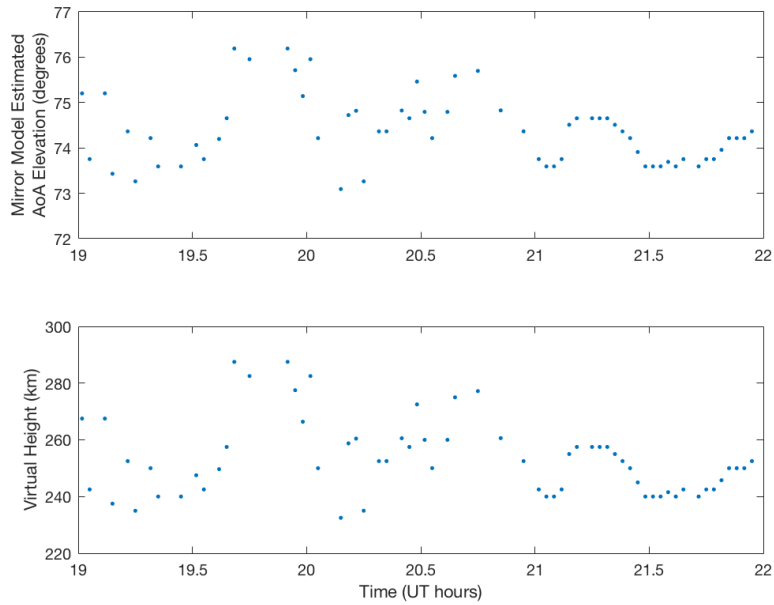
Figure 56. Estimated G10-GRN AoA elevation angles given application of the simple MM using Munyo ionosonde virtual heights during the TID period. Top: Estimated G10-GRN MM AoA elevation angles. Bottom: Munyo ionosonde virtual heights.

calculated from the spectral phase difference in Kirtland and Munyo ionosondes, is $111 \, \mathrm{m \, s^{-1}}$ and the distance between Munyo and G10-GRN midpoint link is 52 km, the time shift is approximately 8 minutes. This time shift is applied to the MM AoA elevation angles and displayed in Figure 58. The time shifted MM is able to predict the overall trend of actual AoA elevation angles through the first half of the TID period; however, the magnitude of the MM elevation angle change does not match the actual measurements, especially after 2030 UT. The difference between the MM and actual AoA elevation angles is shown in Figure 59. Despite only a -0.6° average AoA elevation angle difference, Figure 59 reveals numerous occasions when the differences are greater than 2° and the maximum difference is 6.5° at 2100 UT. Similar to the first analysis at G10-POL, this suggests that the ionospheric tilt, not the height, is responsible for the large changes in AoA elevation angle.

Ionospheric tilt measurements from the Munyo ionosonde are shown in Figure 60,

67
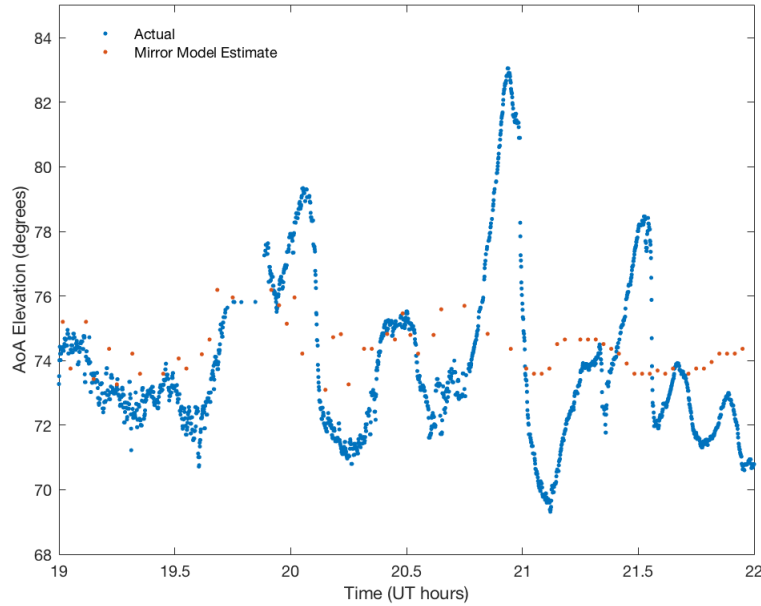
Figure 57. Actual G10-GRN AoA elevation angles along with the simple MM AoA elevation angles. This reveals that the TID passes Munyo prior to the G10-GRN midpoint link; therefore, the MM AOA elevation angles will need to be time shifted to account for the time delay.

along with the difference in G10-GRN MM and actual AoA elevation angles. To evaluate the Munyo North-South tilts against the angle difference, the tilt measurements are also time shifted approximately 8 minutes. Similar to the tilt comparisons at G10-POL, the simple MM does well when the time shifted tilt is near $0°$. This is illustrated in Figure 60 at 1918 UT when the tilt is measured at $0°$ and the angle difference is -0.5°. However, the simple MM does not perform well as the North-South tilt increases, as shown near 2100 UT when the tilt is -4.4° and the error is 6.5°, similar to the results from G10-POL.

To find the maximum change in AoA elevation angles from the simple MM, measurements from Munyo ionosonde virtual heights and G10-GRN AoA actual elevation angles prior to the TID are applied to Equation 14. The initial AoA elevation angle, ϵ_0, is 72.9°, revealing a maximum change in AoA elevation angle of 3.0°. The

68
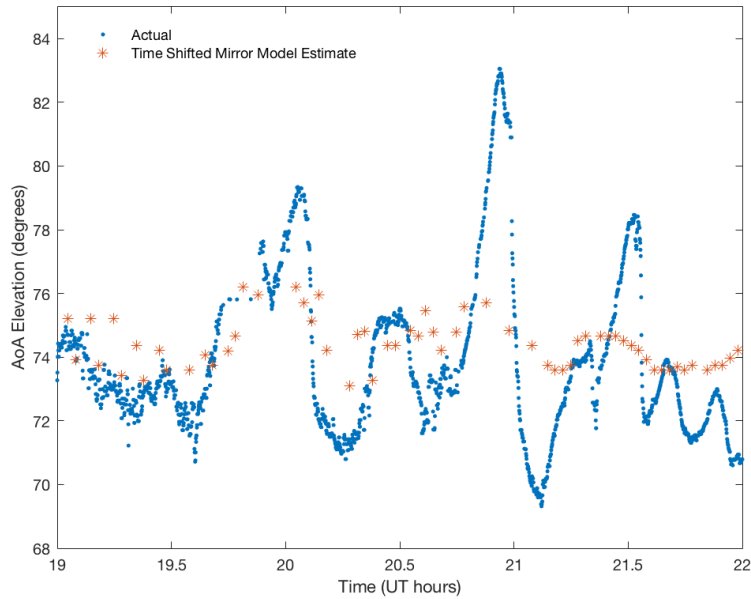
Figure 58. MM AoA elevation angles from Figure 57 are time shifted based on the TID velocity and distance between Munyo and G10-GRN. The time shift allows both data sets to be compared when the TID over the G10-GRN midpoint link.
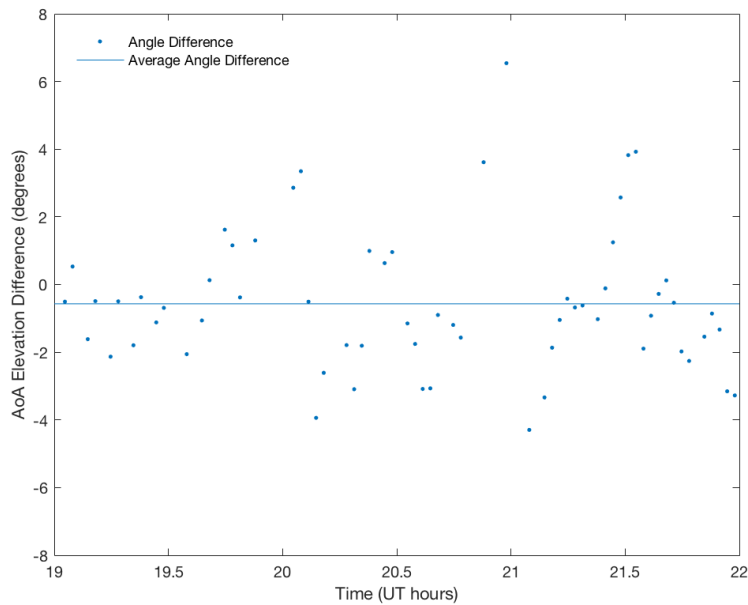
Figure 59. Difference in G10-GRN actual and time shifted MM AoA elevation angles during a TID. The average angle difference highlighted by the solid line is -0.6°.

69
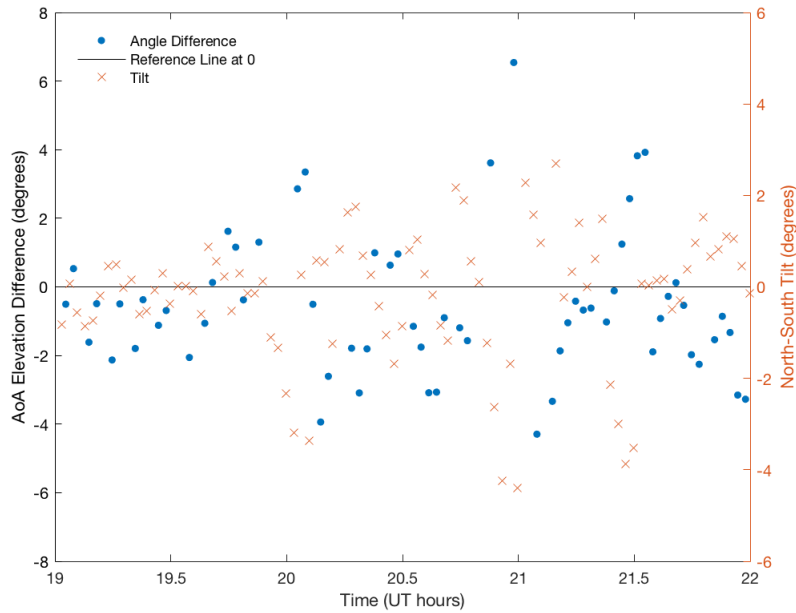
Figure 60. Comparison of the simple MM for G10-GRN with the time shifted Munyo ionosonde North-South tilt measurements. When the tilt is near 0° (horizontal reference line), the angle difference in the MM and actual AoA elevation angles is small as shown at 1918 UT. However, as the tilt increases, so does the error.

time shifted MM AoA elevation angles change by a total of 2.6°, and the actual AoA elevation angles change by a total of 8.6° (Figure 58). Equation 14 overestimates the maximum change in time shifted MM AoA elevation angles by 0.4°, and underestimates the maximum actual AoA elevation angle by 5.6°. Similar to the analysis at G10-POL, the tilt of the ionosphere plays a significant role in influencing AoA elevation angles during a TID.

IV.   Conclusion

Ionospheric measurements of TIDs observed during the IARPA HFGeo field campaign at WSMR in January 2014 were analyzed and compared. TIDs cause large perturbations in the local electron density profile and impact HF radio wave propagation, making geolocation particularly difficult. This research investigated AoA elevation angle and ionosonde virtual height measurements during a TID. The correlation of AoA elevation angle and ionosonde virtual heights were examined, and TID wave characteristics were extracted. Analysis of the TID velocity, period, and wavelength characterized the TID as a MSTID. From the TID velocity, the impact time on a downstream AoA circuit was calculated. Finally, it was determined that a simple MM can predict a change in AoA elevation angle with measurements from two upstream ionosondes given the ionosonde tilt measurement is near $0°$.

To analyze the correlation between AoA elevation angles and ionosonde virtual heights, a simple MM was applied to the AoA elevation angle to obtain the MM height. The results of the simple MM found that AoA MM heights were acceptable on the quiet day, even as reflection heights fluctuated approximately 100 km. However, the TID period revealed AoA MM heights that were 1.2 to 2.3 times higher than the ionosonde virtual heights, and reached reflection altitudes that were not realistic of the 5.34 MHz frequency. Therefore, a correlation of AoA elevation angles and ionosonde virtual heights was performed so no data conversion was required. As the distance between the AoA link midpoint and ionosonde increased, the correlation between measurements decreased with an e-folding distance of 37 km.

A Fourier transform was applied to the AoA and ionosonde data to extract wave characteristics of the TID, which revealed the amplitude and phase as a function of period as the TID propagated from north to south. The spectral analysis of the AoA elevation angles highlighted little change in the amplitude of the wave over a 30

71

minute period, as the TID traveled 33 km from the northern to southern most AoA circuit midpoint. However, the spectral analysis of the four ionosondes, showed the dominant amplitude of the TID ranged from a 36 to 60 minute period depending on the ionosonde location. The TID amplitude and period changed substantially as the wave propagated south over the 288 km distance between the northern and southern most ionosondes. Therefore, the TID measured over Kirtland did not possess the the same characteristics as the TID observed at Squirt.

The TID velocity was measured using ionogram, spectral phase difference, and temporal cross-correlation techniques. The first technique used to compute the TID velocity involved analyzing ionograms for hook signatures. Evaluation of ionograms from each of the four ionosondes revealed the time the hook was first observed. Given the distance between two ionosondes, and the time difference in when the hook was first observed, the TID velocity was calculated. An average of the ionogram velocity measurements revealed a TID velocity of $184\,\mathrm{m\,s^{-1}}$. The second technique used to estimate the velocity involved analyzing the spectral phase difference between two ionosondes. The phase difference for the spectral components with 45 and 60 minute periods were extracted for each of the ionosonde pairs to calculate the velocity, resulting in an average TID velocity of $122\,\mathrm{m\,s^{-1}}$. The difference in the ionogram and spectral analysis velocity measurements were too great to determine which method was accurate, thus a third method for estimating the TID velocity was used. The third and final method was based on a temporal cross-correlation of AoA elevation angles, which yielded a TID velocity of $111\,\mathrm{m\,s^{-1}}$. Based on this final analysis, it was concluded that the spectral analysis provided the accurate TID velocity at $122\,\mathrm{m\,s^{-1}}$. The spectral phase difference velocity provides a good after-the-fact assessment of the TID velocity; however if real-time TID velocities are required, consideration of the AoA temporal cross-correlation should used provided the receivers are aligned with

the propagation of the TID.

An average wavelength of 394 km was calculated using the dispersion relationship, where the TID velocities were derived from the spectral phases for the 45 and 60 minute periods. Given the TID period of 36 to 60 minutes, velocity of $122\,\mathrm{m\,s^{-1}}$, and wavelength of 394 km, the TID analyzed on 26 January 2014 from 1900 to 2200 UT, is classified as a MSTID.

A temporal cross-correlation of ionosonde virtual heights was used to analyze the correlation of virtual heights and AoA elevation angles for geographically separated measurements. This analysis found the time shift at Kirtland to be 11 minutes slower than that expected based on the TID velocity; however, the time shifts at Munyo, Squirt, and Cherry were as expected. Additionally, the temporal cross-correlation found that as the distance between the link midpoint and ionosonde increased, the correlation remained weak even after the time shift. The weak correlation and difference in expected and cross-correlation time shifts suggested that as the TID propagated from north to south, the wave characteristics changed. Lastly, this analysis showed that the temporal cross-correlation works well when the ionosonde and AoA link midpoint are separated by less than 75 km.

To determine if measurements from an upstream ionosonde can be used to predict a change in AoA elevation angle for a downstream midpoint link, a simple MM was applied to ionosonde virtual heights providing the corresponding MM AoA elevation angles. A time shift was applied to the MM AoA elevation angles to account for both the TID velocity and geographical separation between ionosonde and AoA midpoint. The simple MM was able to predict the trend in AoA elevation angles early on; however, the magnitude of the MM AoA elevation angles did not match the actual AoA elevation angle magnitude. This suggests that the tilt of the ionosphere, not the virtual height as the simple MM assumed, is primarily responsible for the large

73

changes in AoA elevation angles. This was further verified when the time shifted ionosonde North-South tilt measurements were compared with the difference in MM and actual AoA elevation angles. When the tilt was near 0°, the difference was very small and the simple MM performed well. However, as the North-South tilt increased, so did the difference in predicted and measured elevation angles, which indicated a poor performance in the simple MM. A comparison of the predicted maximum change in AoA elevation angle to the time shifted MM and actual AoA elevation angles also revealed the importance of the ionospheric tilt at the reflection point when estimating AoA elevation angles.

At the present time, the simple MM is not ready for implementation in geolocation. The simple MM works well when the tilt is near 0° and the HF transmitter coordinates are provided. However, in geolocation the transmitter location is unknown; therefore, the midpoint distance between transmitter and receiver is undetermined and the simple MM cannot be employed. There is a potential to use multiple HF receivers to estimate a midpoint distance and this should be explored in future research.

Additional future research should incorporate the AoA azimuth angle and ionosonde East-West tilt measurements with the simple MM, as this project was only able to evaluate the AoA elevation angle, ionosonde virtual height, and North-South tilt measurements. When this information is bundled together, we expect the simple MM to predict the correct AoA when the overall tilt is 0° during a TID.

Bibliography

Crowley et al., 2013. Crowley, G., Azeem, I., Reynolds, A., Santana, J., and Qian, W. (2013). "Nighttime Medium-Scale Traveling Ionospheric Disturbance (MSTID) in GPS TEC Measurements". *Proceedings of the 2013 International Technical Meeting of the Institute of Navigation*, pages 571–578.

Crowley and Rodrigues, 2012. Crowley, G. and Rodrigues, F. S. (2012). "Characteristics of Traveling Ionospheric Disturbances Observed by the TIDDBIT Sounder". *Radio Science*, 47(3):1–12.

Dao, 2018. Dao, E. (2018). private communication.

Dao et al., 2016. Dao, E. V., McNamara, L. F., and Colman, J. J. (2016). "Magnetic Field Effects on the Accuracy of Ionospheric Mirror models for Geolocation". *Radio Science*, 51(4):284–300.

Davies, 1990. Davies, K. (1990). *Ionospheric Radio.* Peter Peregrinus LTD, London.

Ding et al., 2007. Ding, F., Wan, W., Ning, B., and Wang, M. (2007). "Large-Scale Traveling Ionospheric Disturbances Observed by GPS Total Electron Content During the Magnetic Storm of 29-30 October 2003". *Journal of Geophysical Research: Space Physics*, 112(6):1–15.

Galkin and Reinisch, 2011. Galkin, I. A. and Reinisch, B. W. (2011). "Global Ionospheric Radio Observatory (GIRO)". *Earth Planet Sp*, 63(4):377–381.

Galushko, 2003. Galushko, V. G. (2003). "Frequency-and-Angular HF Sounding and ISR Diagnostics of TIDs". *Radio Science*, 38(6):1–9.

Headrick and Skolnik, 1974. Headrick, J. and Skolnik, M. (1974). "Over-the-Horizon Radar in the HF Band". *Proceedings of the IEEE*, 62(6):664–673.

Hines, 1960. Hines, C. (1960). "Internal Atmospheric Gravity Waves at Ionospheric Heights". *Canadian Journal of Physics*, 38(11):1441–1481.

Hocking, 2001. Hocking, W. (2001). "Buoyancy (gravity) Waves in the Atmosphere". `http://www.physics.uwo.ca/~whocking/p103/grav_wav.html`. [Retrieved on 27 May 2017].

Hunsucker, 1982. Hunsucker, R. D. (1982). "Atmospheric Gravity Waves Generated in the High-Latitude Ionosphere: A Review". *Reviews of Geophysics*, 20(2):293–315.

Kelley, 2009. Kelley, M. C. (2009). *The Earth's Ionosphere: Plasma Physics and Electrodynamics*. Elsevier, Burlington, MA, 2nd edition.

LDI, 2009. LDI (2009). "Lowell Digisonde International: Technical Manual Operation and Maintenance". `http://www.digisonde.com/dps-4dmanual.html`. [Retrieved on 8 May 2017].

MathWorks, 2017. MathWorks (2017). "Curve Fitting Toolbox User 's Guide". `https://www.mathworks.com/help/pdf_doc/curvefit/curvefit.pdf`. [Retrieved on 30 December 2017].

McNamara, 1991. McNamara, L. F. (1991). *The Ionosphere: Communications, Surveillance, and Direction Finding*. Krieger Publishing Company, Malabar, Florida.

Munton et al., 2016. Munton, D., Calfas, R., Gaussiran, T., Rainwater, D., Fleischmann, A., and Schofield, J. (2016). "A Mid-Latitude Skywave Propagation Experiment: Overview and Results". AGU Fall Meeting, San Francisco, December 2016.

76

Nickisch et al., 2016. Nickisch, L. J., Fridman, S., Hausman, M., Kraut, S., and Zu-nich, G. (2016). "Assimilative Modeling of Ionospheric Dynamics for Nowcasting of HF Propagation Channels in the Presence of TIDs". *Radio Science*, 51(3):184–193.

Otsuka et al., 2013. Otsuka, Y., Suzuki, K., Nakagawa, S., Nishioka, M., Shiokawa, K., and Tsugawa, T. (2013). "GPS Observations of Medium-Scale Traveling Iono-spheric Disturbances Over Europe". *Annales Geophysicae*, 31(2):163–172.

Paznukhov et al., 2012. Paznukhov, V. V., Galushko, V. G., and Reinisch, B. W. (2012). "Digisonde observations of TIDs with frequency and angular sounding tech-nique". *Advances in Space Research*, 49.

Pisacane, 2008. Pisacane, V. (2008). *The Space Environment and its Effects on Space Systems*. American Institute of Aeronautics and Astronautics, Reston, Virginia.

Reinisch, 2017. Reinisch, B. (2017). "Global Map of GIRO Digisondes". `http://www.digisonde.com/digisonde-station-map.html`. [Retrieved on 11 November 2017].

Schunk and Nagy, 2009. Schunk, R. W. and Nagy, A. F. (2009). *Ionospheres: Physics, Plasma Physics, and Chemistry*. Cambridge University Press, New York, second edi edition.

Shiokawa et al., 2002. Shiokawa, K., Otsuka, Y., Ogawa, T., Balan, N., Igarashi, K., Knipp, D. K., Ridley, A. J., Saito, A., and Yumoto, K. (2002). "Com-prehensive observations of large-scale traveling ionospheric disturbances during the magnetic storm of September 15, 1999". *J. Geophys. Res.*, 107(September 1999):10.1029/2001JA00245.

Tedd et al., 1984. Tedd, B., Morgan, M., and Ballard, K. (1984). "The Height De-pendence of TID and Gravity Wave Parameters". *Journal of Geophysical Research*, 89(A10):9023–9033.

Walterscheid et al., 2003. Walterscheid, R. L., Schubert, G., and Brinkman, D. G. (2003). "Acoustic Waves in the Upper Mesosphere and Lower Thermosphere Generated by Deep Tropical Convection". *Journal of Geophysical Research: Space Physics*, 108(A11).

REPORT DOCUMENTATION PAGE

The public reporting burden for this collection of information is estimated to average 1 hour per response, including the time for reviewing instructions, searching existing data sources, gathering and maintaining the data needed, and completing and reviewing the collection of information. Send comments regarding this burden estimate or any other aspect of this collection of information, including suggestions for reducing this burden to Department of Defense, Washington Headquarters Services, Directorate for Information Operations and Reports (0704–0188), 1215 Jefferson Davis Highway, Suite 1204, Arlington, VA 22202–4302. Respondents should be aware that notwithstanding any other provision of law, no person shall be subject to any penalty for failing to comply with a collection of information if it does not display a currently valid OMB control number. **PLEASE DO NOT RETURN YOUR FORM TO THE ABOVE ADDRESS.**

1. REPORT DATE (DD–MM–YYYY)	2. REPORT TYPE	3. DATES COVERED (From — To)
22–03–2018	Master's Thesis	May 2016 — Mar 2018

4. TITLE AND SUBTITLE

A Comparison of High Frequency Angle of Arrival and Ionosonde Data During a Traveling Ionospheric Disturbance

5a. CONTRACT NUMBER

5b. GRANT NUMBER

5c. PROGRAM ELEMENT NUMBER

6. AUTHOR(S)

Knippling, Kalen L, Capt, USAF

5d. PROJECT NUMBER

5e. TASK NUMBER

5f. WORK UNIT NUMBER

7. PERFORMING ORGANIZATION NAME(S) AND ADDRESS(ES)

Air Force Institute of Technology
Graduate School of Engineering and Management (AFIT/EN)
2950 Hobson Way
WPAFB OH 45433-7765

8. PERFORMING ORGANIZATION REPORT NUMBER

AFIT-ENP-MS-18-M-087

9. SPONSORING / MONITORING AGENCY NAME(S) AND ADDRESS(ES)

Air Force Research Laboratory/Space Vehicles
3550 Aberdeen Avenue SE
Kirtland AFB, NM 87117
DSN 246-3172, COMM 505-846-3172
Email: jonah.colman.1@us.af.mil

10. SPONSOR/MONITOR'S ACRONYM(S)

AFRL/RV

11. SPONSOR/MONITOR'S REPORT NUMBER(S)

12. DISTRIBUTION / AVAILABILITY STATEMENT

Distribution Statement A:
Approved for Public Release; distribution unlimited.

13. SUPPLEMENTARY NOTES

This work is declared a work of the U.S. Government and is not subject to copyright protection in the United States.

14. ABSTRACT

High Frequency (HF) geolocation techniques are commonly used to track the source of uncooperative HF emitters. A traveling ionospheric disturbance (TID) makes geolocation particularly difficult due to large perturbations in the local ionospheric electron density profile. Angle of arrival (AoA) and ionosonde virtual height measurements collected at White Sands Missile Range, New Mexico in January 2014, are analyzed during a medium scale traveling ionospheric disturbance. TID characteristics are extracted from the measurements, and a comparison between the data sets is performed to provide a measure of correlation as a function of distance and time between the ionosonde and AoA circuit midpoints. Additionally, ionosonde measurements are used in a simple model to predict AoA elevation angle changes at a downstream HF receiver. The simple model is able to predict changes in AoA elevation angles when the ionosonde North-South tilt is zero; however, as the tilt increases, so too does the error in the simple model.

15. SUBJECT TERMS

angle of arrival, traveling ionospheric disturbance, ionosonde, geolocation

16. SECURITY CLASSIFICATION OF:			17. LIMITATION OF ABSTRACT	18. NUMBER OF PAGES	19a. NAME OF RESPONSIBLE PERSON
a. REPORT	b. ABSTRACT	c. THIS PAGE			Maj Daniel J. Emmons, AFIT/ENP
U	U	U	UU	97	**19b. TELEPHONE NUMBER** (include area code) 937-255-3636x4571; daniel.emmons@afit.edu